공학박사 학위논문

Bio-inspired artificial vision and neuromorphic imaging devices

생체모방 인공 시각 및 뉴로몰픽 이미징 디바이스

2022 년 2 월

서울대학교 대학원

화학생물공학부 에너지환경 화학융합기술전공

김 민 성

Bio-inspired artificial vision and neuromorphic imaging devices

지도 교수 김 대 형

이 논문을 공학박사 학위논문으로 제출함
2022 년 2 월

서울대학교 대학원
화학생물공학부 에너지환경 화학융합기술전공
김 민 성

김 민 성 의 공학박사 학위논문을 인준함
2022 년 2 월

위 원 장 _____ 성 영 은 _____ (인)

부위원장 _____ 김 대 형 _____ (인)

위   원 _____ 현 택 환 _____ (인)

위   원 _____ 송 영 민 _____ (인)

위   원 _____ 손 동 희 _____ (인)

Abstract

Bio-inspired artificial vision and neuromorphic imaging devices

Min Sung Kim

School of Chemical and Biological Engineering

Chemical Convergence for Energy & Environment

The Graduate School

Seoul National University

In the past decade, significant advancements have been accomplished in image sensor technology for achieving efficient object detection with high signal to noise ratio that consists of image acquisition and image data processing. This advancement in image capturing and image processing has promoted major development in the field of mobile electronics and applications in machine vision. However, since the conventional imaging technology uses a planar image sensor, a multi-lens structure is required for wide visual field, high-quality and aberration-free imaging. This multi-lens structure makes the camera module large and bulky, which

hinders the miniaturization of overall system. In this context, by mimicking a single lens and a curved retina structure of natural eyes that evolved to be optimized for their habitat, such technological limitations can be efficiently resolved. Also, by mimicking their strategies to obtain high quality visual information in their habitat, specialized camera with high object detectability and high signal to noise ratio can be developed. Here, we describe three different types of the next-generation bio-inspired artificial vision systems.

Firstly, we develop a novel wide-field-of-view camera by integrating a tailored monocentric lens and a hemispherical silicon nanorod photodiode array inspired by the eye of an aquatic animal. Such an aquatic-vision-inspired camera offers the wide FoV, miniaturized module size, minimal optical aberration, deep depth-of-field, facile accommodation, and enhanced light sensitivity in one simple integrated device. Theoretical analyses and imaging demonstrations have corroborated the validity of the developed artificial vision system.

Secondly, inspired by the cuttlefish-eye, we develop a high-contrast polarizing camera that specializes in the low-contrast shallow-water environment. By mimicking the W-shaped pupil of cuttlefish-eye, an artificial vision system compensates uneven vertical light profile. In addition, the cylindrical silicon photodiode array which contains high-density belt-like pixel profile, allowing to have wide horizontal-field-of-view inspired by curved retina of cuttlefish-eye. The flexible, linear polarizing film on top of the cylindrical silicon photodiode array enables high-contrast polarization imaging.

Thirdly, inspired by the structural and functional features of the human visual recognition system, we report a curved neuromorphic image sensor array with reduced noise by employing a heterostructure of MoS_2 and poly(1,3,5-trimethyl-1,3,5-trivinyl cyclotrisiloxane) (pV3D3). Such an artificial vision system features the photon-triggered electrical responses similar to the synaptic plasticity of neural network that consists of short-term plasticity and long-term potentiation. Such photon-triggered synaptic plasticity of the MoS_2-pV3D3 phototransistor was experimentally and theoretically analyzed. The developed system can efficiently recognize the original image by reducing the noises of input images.

Keywords: Bio-inspired artificial vision, Artificial synapse, specialty camera, Curved image sensor, Neuromorphic vision sensor, Flexible electronics

Student number: 2016-20992

Contents

List of Figures

Chapter 1

Chapter 2

Chapter 3

Chapter 4

Chapter 1. Introduction

1.1 Evolution of efficient imaging and image processing technologies

Technological advances in mobile electronics and machine vision has boosted the demand for advanced devices for image acquisition and processing[1,2]. However, conventional imaging and image processing systems using a flat image sensor array, a multi-lens optics and the von-Neumann computing architecture have some limitations, which are high system-level complexity, large module size, heavy computing load, and low energy efficiency[3]. Thus, devices that can acquire image and process image data, simultaneously, are required. As a result, bio-inspired imaging devices[4] and neuromorphic image processing devices[5] have attracted great attention (Fig. 1.1).

Bio-inspired artificial vision systems for image acquisition have been studied in the past decades[6]. Conventional imaging devices require complicated optics to secure high-quality vision[7]. In contrast, the eyes in nature have a quite simple optics with high-quality vision[8]. Thus, by mimicking the structural and functional features of the eyes in nature, bio-inspired cameras have been developed[2] (Fig. 1.1a). For instance, the chambered eye that is a typical type of eyes found in humans and aquatic animals, shows a simple optics with wide visual field, low optical aberration, and facile accommodation[9].

Devices for neuromorphic computing that can process a large amount of image data that is obtained with the imaging devices have been studied for efficient image processing[10]. The conventional von-Neumann computing architecture is unsuitable for efficient processing of the massive image information, because the central processing unit and memory unit are separated[11]. Therefore, advanced computing devices that are inspired by the brain of human have been developed[12] (Fig. 1.1b). For example, the memristor crossbar arrays that can conduct vector multiplications efficiently have been developed[13]. Such devices that adapt hardware implementation of artificial neural networks (ANN) enable parallel image data processing with very low energy consumption[12].

However, such devices still need additional image sensor arrays for image data acquisition[14]. The addition of image sensor array introduces high system-level complexity[15]. Therefore, integration of an image sensor array and a neuromorphic image processing device has been developed[16] (Fig. 1.1c). The neuromorphic image processing device shows synaptic behavior in response to the light, which are short-term plasticity (STP), long-term plasticity (LTP), and spike-timing-dependent plasticity (STDP)[16]. Also, by mimicking the visual system of human, neuromorphic image processing devices that can conduct image pre-processing[17] and image post-processing[18] have been proposed.

In this section, we review recent progresses in the bio-inspired artificial vision and neuromorphic image processing devices, aiming to efficiently recognize the image data. First, we discuss the bio-inspired imaging devices that emulate structural and functional features of the eyes of nature which are chambered eyes.

Second, we introduce the artificial synapses, which are inspired by efficient image processing of human brain. Third, we propose the neuromorphic vision sensor, which integrates the image acquisition and neuromorphic image data processing functions in a one device. Finally, we summarize the recent progresses of the aforementioned devices.
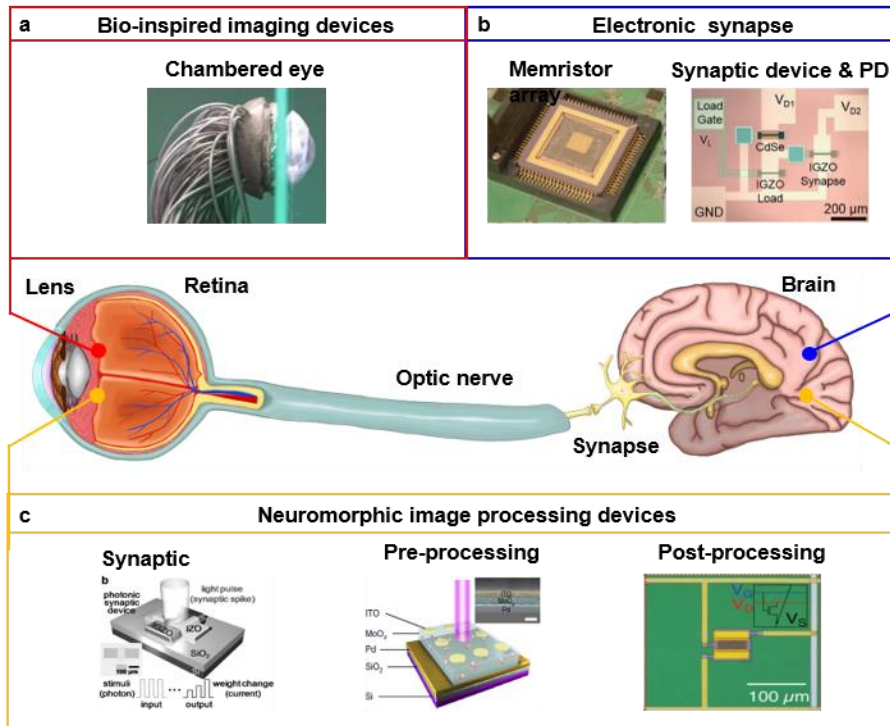
Figure 1.1. Various imaging devices and image processing devices inspired by the visual system of human. (a) Bio-inspired artificial vision[19], **(b)** Electronic synapse[12,20], and **(c)** Neuromorphic vision sensor[16,17,18].

1.2 Bio-inspired artificial vision system inspired by the chambered eye

Mimicking the structural and functional advantages of the eyes of nature can be a suitable solution to solve the technological problems of the conventional imaging systems. This section discusses the distinctive imaging systems that are inspired by various natural eyes, such as a chambered eye.

1.2.1 Human eye system

The chambered eye is a typical eye type found in human and aquatic animals. It consists of a single lens and a curved retina[21], and shows high-quality visions[6], such as wide visual field, low optical aberration, and facile accommodation. The optical component of the chambered eye has evolved to optimize in its habitat[22]. For example, the human eye has an aspherical crystalline lens with a graded refractive index (GRIN) for compensating the optical aberrations[23].

The chambered eye has a curved retina that enables high-resolution imaging with a wide visual field and low optical aberrations with a simple optics[22] (Fig. 1.2a). Recently, many studies to realize artificial curved retina have been reported, which are mesh-type array[24], thin complementary metal-oxide-semiconductor (CMOS) image sensor array[25], and origami and kirigami image sensor array methods[26].

An electronic eye, based on a curved silicon image sensor array and an isolated pixel design has been reported[27] (Fig. 1.2b). Conventional fabrication processes are applied to manufacture a passive matrix image sensor array based on silicon photodiodes, blocking diodes, metal electrodes, and polyimide (PI) encapsulation. The compressible metal interconnection enables to transfer the flat device to a curved substrate (Fig. 1.2c). Under reverse bias, the I-V curve of silicon image sensor array shows a typical truncated shape of bipolar junction transistor with a high on/off ratio (Fig. 1.2d).

As an another strategy to fabricate the curved image sensor array, the serpentine-shaped metal interconnection can be applied to enhance mechanical flexibility[28]. The serpentine-shaped interconnection enables such an image sensor

array to be more stretchable and flexible[29]. Thus, it can be conformally contacted on the curved surface (Fig. 1.2e). However, such a serpentine-shaped array design still suffers from a low pixel density. Therefore, unique strategy for overcoming such a low pixel density issue is still required. For instance, a human-eye-inspired curved image sensor array using a heterostructure of MoS_2 and graphene with the kirigami design has been developed[30] (Fig. 1.2f). The kirigami-type array design enables to transfer-print the high-density curved image sensor array from a flat surface to a curved surface with the minimized mechanical failure[26]. In addition, the ultrathin device thickness and the use of the soft two-dimensional (2D) materials help to prevent the transfer-printed array from undergoing mechanical fractures. The photodetector shows high photoabsorption efficiency, high photoresponsivity, and minimized fracture strain on a curved surface (Fig. 1.2g).
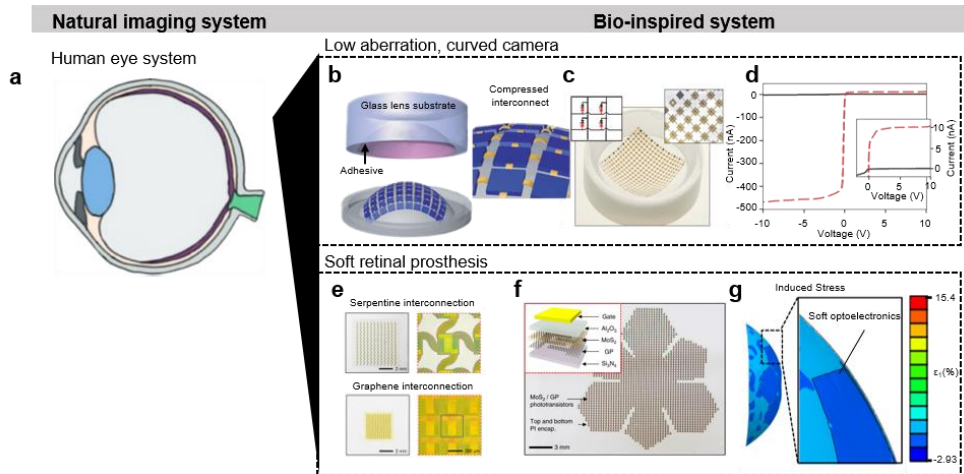
Figure 1.2. Various human-eye-type imaging system. a) Schematic illustration of human eye system. b) Schematic illustration of the fabrication process of the device[27]. c) Schematic illustration of the device[27]. d) I-V characteristics curve[27]. e) Serpentine-type metal interconnection (top) and graphene interconnection (bottom)[30]. f) Optical microscopic image of the device based on MoS$_2$ and graphene[30]. g) Induced strain of the device on the curved surface[30].

8

1.3 Neuromorphic image processing devices

In this chapter, we discuss various neuromorphic image processing devices such as the electronic synapses and neuromorphic vision sensors including pre-processing and post-processing devices.

1.3.1 Electronic synapse

Memristor is a two-terminal electronic device, and its resistance state changes according to the amount of current flowed on the device[5]. When it is arranged in a crossbar array type, it can efficiently conduct vector-multiplication tasks using its programmable conductance states.

A WO_x-based memristor crossbar array that can efficiently recognize the object has been implemented for the sparse coding[12] (Fig. 1.3). Its conductance states can be modulated by reconfiguring ions inside of the WO_x memristor (Fig. 1.3). In addition, the 32×32 crossbar array can conduct the matrix operation according to the Kirchhoff's law (Fig. 1.3c). By using the dictionary elements, the input image in greyscale (Fig. 1.3d) can be converted to the reduced complexity image (Fig. 1.3e). Specifically, a 4×4 patch which is a part of the original input image can be reconfigured as the iteration number increases (Fig. 1.3f).

An artificial synaptic device integrated with a photodetector (Fig. 1.4a) has been developed for efficient pattern and color recognition[31]. The photodetector based on a heterostructure of h-BN and WSe_2 converts the optical inputs with three different wavelengths into the pre-synaptic electrical signals. In addition, such pre-synaptic electrical signals affect the post-synaptic current (Fig. 1.4b). The top surface of the h-BN layer is exposed to the O_2 plasma, and it serves as a weight control layer (WCL). The applied voltage signals lead to trapping of electrons at the WCL–WSe_2 interface. Such trapping and de-trapping process facilitates the linear change of weight, as the conductance state is maintained stably (Fig. 1.4c). Using the parameters extracted from the device during the training process (Fig. 1.4d, left), the

single colored pattern or the color-mixed pattern (Fig. 1.4d, right) were efficiently recognized. The recognition accuracy of the synaptic device with a photodetector was compared to that of a conventional neural network (Fig. 1.4e). With the same training epochs, the recognition rate of the synaptic device with a photodetector was higher than that of the conventional neural network (Fig. 1.4f).
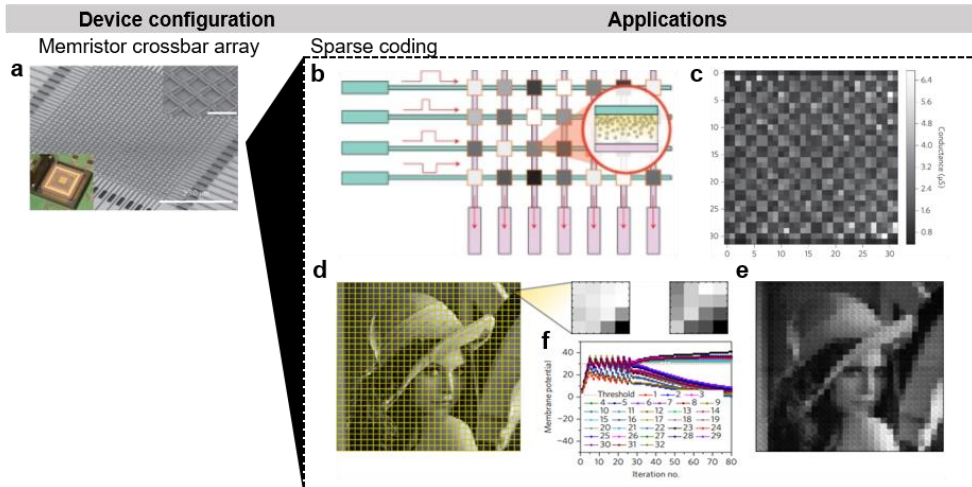
Figure 1.3. The memristor crossbar array and its major applications[12]. (a) Scanning electron microscope (SEM) image of the memristor crossbar array. **(b)** Schematic illustration of device. **(c)** Programmed 32 × 32 patterns. **(d)** Original greyscale image for the image processing. **(e)** Reconstructed image. **(f)** Graph showing membrane potentials of the device as a function of the iteration number.
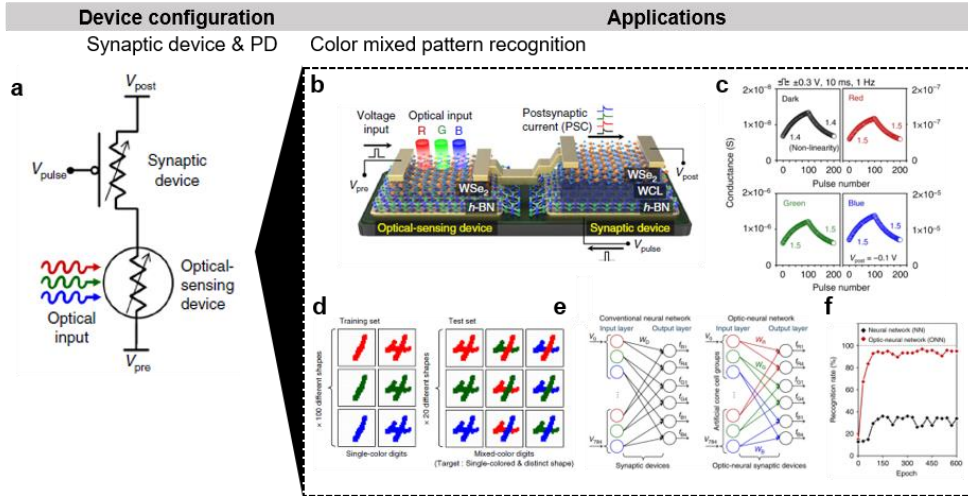
Figure 1.4. The synaptic device integrated with the photodetector and its major applications[31]. (a) Schematic circuit illustration of overall system for the color-mixed pattern recognitions. **(b)** Schematic illustration of the device based on h-BN/WSe$_2$ and h-BN/WCL/WSe$_2$. **(c)** Graph showing conductance change as a function of the pulse number under light of different wavelengths of light. **(d)** Various patterned images for the training and testing process, such as single-color digits and mixed-color digits. **(e)** Schematic illustration of conventional neural network (left) and optic-neural network (right). **(f)** Graph showing recognition rate of neural network and optic-neural network as a function of epochs.

13

1.3.2 Neuromorphic vision sensor and pre-/post-processing devices

A photon-induced neuromorphic vision sensor based on amorphous oxide semiconductors (AOSs) has been developed[16]. Such a two-terminal device shows a persistent photoconductivity under UV irradiation. The extraordinary characteristics of such a device, including the long photocurrent decay time and the long lasting photoconductivity, are presented. Such a persistent photoconductivity is resulted from the excess carrier generation due to the photo-induced ionized oxygen vacancies (Fig. 1.5a). Photon-induced neuromorphic current responses, including STP and LTP, can be presented by modulating the photon energy and the frequency of the optical input pulses (Fig. 1.5b and 1.5c, respectively). In addition, the STDP was shown by using two serially connected synaptic devices (Fig. 1.5d). The strength of connection between the adjacent devices reinforced as the time interval between the pre-synaptic and postsynaptic currents decreased.

Neuromorphic vision sensors that can conduct the image acquisition and image pre-processing in one device were also developed, which is an optoelectronic resistive random-access memory[17]. A two-terminal device structure based on Pd/MoO$_x$/ITO (Fig. 1.6a) shows light-tunable non-volatile switching behaviors that are the high-resistance state (HRS) and low-resistance state (LRS) (Fig. 1.6b). When the MoO$_x$ in the HRS is exposed to UV light, protons (H$^+$) are produced by the reaction between the photogenerated holes and the water molecules. Such a process modifies the resistance state from the HRS to the LRS (Fig. 1.6c, left). When an electrical field is applied, H$^+$ drifts from the MoO$_x$ to the Pd electrode. Such a process modifies the resistance state from the LRS to the HRS (Fig. 1.6c, right). By using

14

such a switching mechanism, the original input image could be pre-processed into an output image with high contrast and reduced noise (Fig. 1.6d). As a result, the image recognition with the proposed system exhibits a higher accuracy than that without the proposed system (Fig. 1.6e).

Neuromorphic vision sensors with image acquisition and image post-processing function in a single device have been also developed[18]. By using large-area MoS_2 monolayer, a 32×32 MoS_2 phototransistor array for the machine vision application has been demonstrated (Fig. 1.7a). Inspired by the main functions of the human visual recognition system, including optical sensing, memory, and recognition, the persistent photoconductivity effects of the MoS_2 transistor (Fig. 1.7b), were demonstrated. The persistent photocurrent is generated in response to optical input, and the conductance states of pixels are modulated by the input light dosage (Fig. 1.7c). In addition, the vector–matrix multiplications are operated by the stored conductance states of pixels for the image recognition tasks (Fig. 1.7d).
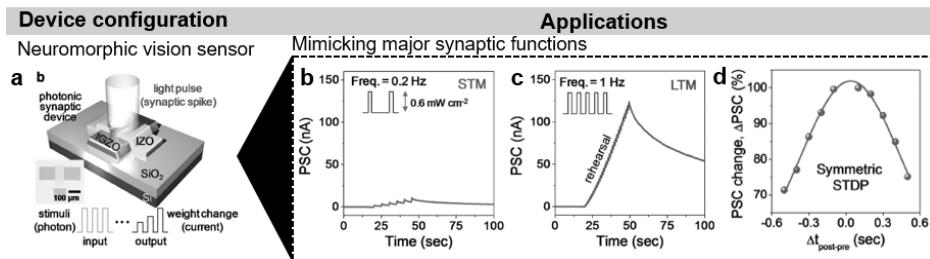
Figure 1.5. Neuromorphic vision sensor[16]. (a) Schematic illustration of the photonic neuromorphic device. (**b,c**) Graph showing postsynaptic current behavior, such as short-term memory (b) and long-term memory (c). **(d)** Graph showing postsynaptic current change as a function of the time interval.
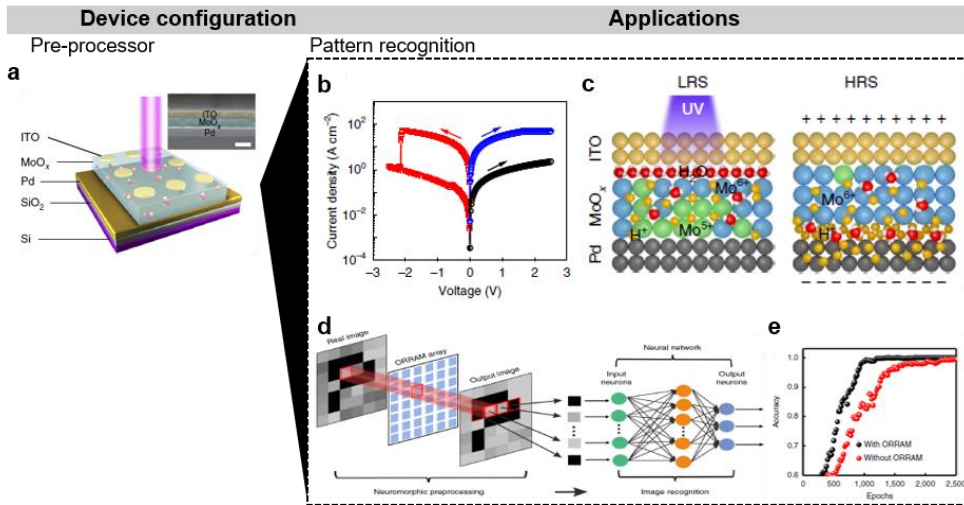
Figure 1.6. Neuromorphic vision sensors for the pre-processing applications[17].
(a) Schematic illustration of the optoelectronic resistive random access memory. **(b)**
I–V characteristic curve of the device. **(c)** Schematic illustration of UV light-induced
resistive switching mechanism of the device. **(d)** Schematic illustration of overall
image recognition process using the device. **(e)** Graph showing the recognition
accuracy of system with and without the device as a function of epochs.
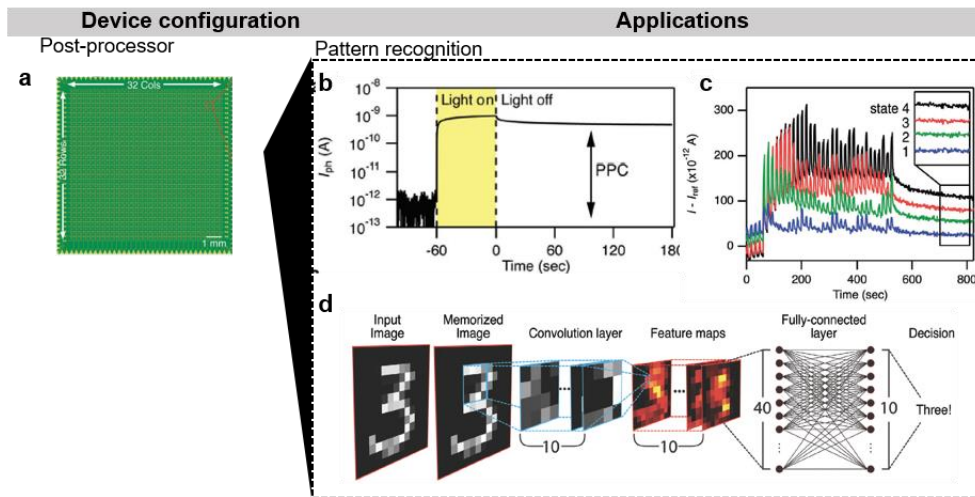
Figure 1.7. Neuromorphic vision sensors for the post-processing applications[18].
(a) Optical microscopy image of the 32×32 MoS$_2$ phototransistor array. **(b)** Transient characteristic curve of the device. **(c)** Graph showing transient characteristics curve of four different optically programmed states. **(d)** Schematic illustration of the overall image recognition process using the device.

1.4 Conclusion

Recent progresses in the development of the image acquisition system and processing system were reviewed. High-quality and multifunctional image acquisition systems inspired by the structural advantages of the eyes of nature and extraordinary computing architectures inspired by the neural network of the human brain have been discussed. The integrated device which is a combination of the front-end image acquisition device and back-end image processing device can considerably improve the system-level efficiency of overall image recognition process. Such distinctive approaches can be highly suitable for the development of the next-generation machine vision devices. These bio-inspired artificial imaging systems and neuromorphic image processing devices are a significant advancement to develop the novel electronic devices.

1.5 Reference

* The contents of this chapter were published in Advanced Materials Technologies, 2021, 2100144.

1. Deng, H. et al. Catadioptric planar compound eye with large field of view. *Opt. Express* **26**, 12455 (2018).

2. Powell, S. B., Garnett, R., Marshall, J., Rizk, C., Gruev, V. Bioinspired polarization vision enables underwater geolocalization. *Sci. Adv.* **4**, eaao6841 (2018).

3. Guo, Q., Alexander, E., Zickler, T. Focal track: Depth and accommodation with oscillating lens deformation. *Proc. IEEE Int. Conf. Comput. Vis.* **2017-Octob**, 966 (2017).

4. Brueckner, A. et al. Thin wafer-level camera lenses inspired by insect compound eyes. *Opt. Express* **18**, 24379 (2010).

5. Xia, Q. F., Yang, J. J. Publisher Correction: Memristive crossbar arrays for brain-inspired computing. *Nat. Mater.* **18**, 518 (2019).

6. Cox, M. J. Optics of the Human Eye. *Ophthalmic Physiol. Opt.* **21**, 426 (2001).

7. Posch, C., Serrano-Gotarredona, T., Linares-Barranco, B., Delbruck, T. Retinomorphic Event-Based Vision Sensors: Bioinspired Cameras With Spiking Output. *Proc. Ieee* **102**, 1470 (2014).

8. Land, M. F. The optics of animal eyes. *Contemp. Phys.* **29**, 435 (1988).

9. Lakshminarayanan, V., Kuppuswamy Parthasarathy, M. Biomimetic optics: visual systems. *J. Mod. Opt.* **0340**, 1 (2016).

10. Lin, P. et al. Three-dimensional memristor circuits as complex neural networks. *Nat. Electron.* **3**, 225 (2020).

11. Zidan, M. A., Strachan, J. P., Lu, W. D. The future of electronics based on memristive systems. *Nat. Electron.* **1**, 22 (2018).

12. Sheridan, P. M. et al. Sparse coding with memristor networks. *Nat. Nanotechnol.* **12**, 784 (2017).

13. Jo, S. H. et al. Nanoscale Memristor Device as Synapse in Neuromorphic Systems. *Nano Lett.* **10**, 1297 (2010).

14. Zhou, F., Chen, J., Tao, X., Wang, X., Chai, Y. 2D Materials Based Optoelectronic Memory: Convergence of Electronic Memory and Optical Sensor. *Research* **2019**, 1 (2019).

15. Choi, C. et al. Curved neuromorphic image sensor array using a MoS_2-organic heterostructure inspired by the human visual recognition system. *Nat. Commun.* **11**, 5934 (2020).

16. Lee, M. et al. Brain-Inspired Photonic Neuromorphic Devices using Photodynamic Amorphous Oxide Semiconductors and their Persistent Photoconductivity. *Adv. Mater.* **29**, 1700951 (2017).

17. Zhou, F. C. et al. Optoelectronic resistive random access memory for neuromorphic vision sensors. *Nat. Nanotechnol.* **14**, 776 (2019).

18. Jang, H. et al. An Atomically Thin Optoelectronic Machine Vision Processor. *Adv. Mater.* **32**, 2002431 (2020).

19. Gu, L. L. et al. A biomimetic eye with a hemispherical perovskite nanowire array retina. *Nature* **581**, 278 (2020).

20. Kwon, S. M. et al. Environment-Adaptable Artificial Visual Perception Behaviors Using a Light-Adjustable Optoelectronic Neuromorphic Device Array. *Adv. Mater.* **31**, 1906433 (2019).

21. Zuccarello, G., Scribner, D., Sands, R., Buckley, L. J. Materials for Bio-inspired Optics. *Adv. Mater.* **14**, 1261 (2002).

22. Ji, S. Z. et al. A bio-inspired polymeric gradient refractive index (GRIN) human eye lens. *Opt. Express* **20**, 26746 (2012).

23. Beadie, G. et al. Tunable polymer lens. *Opt. Express* **16**, 11540 (2008).

24. Kim, H. M., Lee, G. J., Kim, M. S., Song, Y. M. Fabrication of Flexible Image Sensor Based on Lateral NIPIN Phototransistors. *J. Vis. Exp.* DOI 10.3791/57502 (2018).

25. Guenter, B. et al. Highly curved image sensors: a practical approach for improved optical performance. *Opt. Express* **25**, 13010 (2017).

26. Zhang, K. et al. Origami silicon optoelectronics for hemispherical electronic eye systems. *Nat. Commun.* **8**, 1782 (2017).

27. Ko, H. C. et al. A hemispherical electronic eye camera based on compressible silicon optoelectronics. *Nature* **454**, 748 (2008).

28. Sim, K. et al. Three-dimensional curvy electronics created using conformal additive stamp printing. *Nat. Electron.* **2**, 471 (2019).

29. Cho, K. W. et al. Large scale and integrated platform for digital mass culture of anchorage dependent cells. *Nat. Commun.* **10**, 4824 (2019).

30. Choi, C. et al. Human eye-inspired soft optoelectronic device using high-density MoS2-graphene curved image sensor array. *Nat. Commun.* **8**, 1664 (2017).

31. Seo, S. et al. Artificial optic-neural synapse for colored and color-mixed pattern recognition. *Nat. Commun.* **9**, 5106 (2018).

Chapter 2. An aquatic-vision-inspired camera based on a monocentric lens and a silicon nanorod photodiode array

2.1 Introduction

Next-generation mobile electronics has driven the advancement of wide visual field, miniaturized cameras, in particular, for avoiding obstacles and tracking object[1]. However, the large Petzval field curvature for the imaging in wide visual field requires for multi-lenses to clearly focus the images on a flat image sensor array[3]. Such requirements inevitably increase the size and weight of the camera[3]. For instance, the conventional wide visual field camera (Field-of-view > 120°) needs a large number of lenses[5].Thus, such a multi-lenses optics results in the bulky and heavy system configuration.

The natural eyes are optimized through evolution, and have promoted the development of extraordinary bio-inspired cameras[6]. For instance, human-eye-inspired curved image sensor array that is integrated with a plano-convex lens has facilitates less optical aberration imaging[9]. However, such bio-inspired cameras have limited visual field, which is around 100°, because of large off-axis aberrations in large angles[3]. Further, the human eye system is not a single-lens system, because it needs an additional refractive lens, which is a cornea, to reduce the optical aberrations[12]. In another example, the compound-eye-type optics has shown the wide

visual field features[13] (Fig. 2.1). However, they have poor clarity of vision than the chambered-eye-type[3], which are the eyes of vertebrates and aquatic animals, because miniaturization of their corneal micro-lens is limited due to their small diffraction limit.

Instead, the aquatic eyes of fish[17], cephalopods[18], and aquatic mammals[19], have the wide visual field and high visual acuity features with the simple optics[5], minimized optical aberrations[18], deep depth-of-field (DoF)[20], and facile accommodation[21](Fig. 2.2). In addition, photoreceptors of aquatic visions exhibit the high light sensitivity, enabling the high visual acuity in the dim underwater environment[22]. Such features of the aquatic eyes are resulted from a spherical monocentric lens (*mo*-lens) with a parabolic refractive index (RI) distribution[5,17] and a hemispherical retina with light-sensitive elongated rod cells[23]. Such structural and functional advantages of the aquatic eyes have promoted the advancement of a next-generation wide field of view system for the novel mobile electronics[24,25].

Herein, by applying the optical features of the aquatic eyes, we report a bio-inspired artificial vision by integrating a tailored *mo*-lens and a hemispherical silicon nanorod photodiode array (*h-SiNR*-PDA). Such an aquatic-vision-inspired artificial vision have wide visual field around 120°, small form factor around 11.5 mm, minimized optical aberrations, deep DoF, and facile visual accommodation. Further, the *h-SiNR*-PDA shows a high-quality imaging under vignetting with improved light sensitivity due to the nanotextured surface and surface passivation of the silicon photodiode. The aquatic-vision-inspired artificial vision has enabled all

25

aforementioned advantages in one single device, and can obtain the wide visual field input images.

Compound-eye-inspired camera

Wide visual field

Corneal
micro-lens

Photodetectors
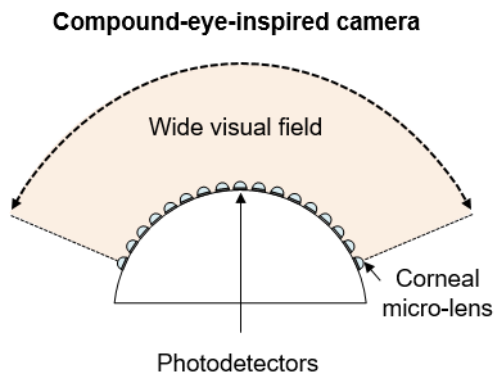
Figure 2.1. Compound-type-eye structure.
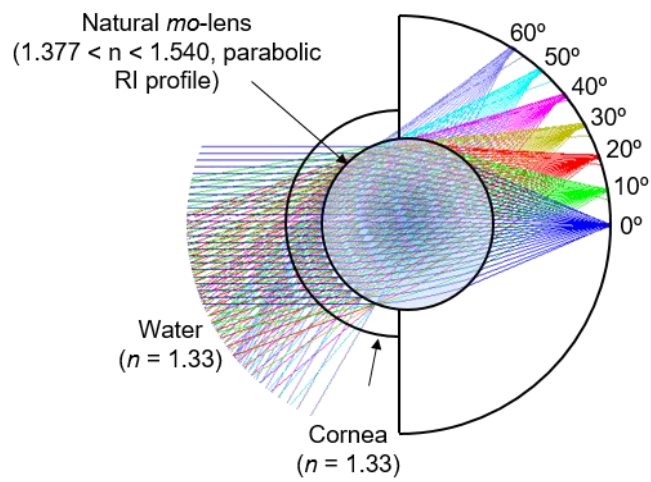
Figure 2.2. An aquatic-type-eye structure.

2.2 Experimental Section

2.2.1. Fabrication process and characterizations of the monocentric lens.

To manufacture the monocentric lens, two different sorts of lens, that are BK7 and SF16, were employed. The RIs, which are characterized at $\lambda = 588$ nm, and the radius of curvature of BK7 are 1.52 and 2 mm, respectively. The RIs, which are characterized at $\lambda = 588$ nm, and the radius of curvature of SF16 are 1.65 and 4.1 mm, respectively. A transparent optical adhesive (NOA 61, Norland Products) whose RI is 1.56 was employed for filling the gap between lenses. Their surface profiles were inspected by a large-area aspheric 3D profiler (UA3P, Panasonic).

Fabrication process of the monocentric lens (Fig. 2.3) started with the drop-coating of NOA 61 on BK7 (half-ball lens). The BK7 was then placed on the aperture by using an automated centering machine. Then, NOA 61 was optically-cured by irradiate UV, in order to fix the BK7 on the aperture. The gap between the BK7 and the aperture was filled by using NOA 61. Then, another BK7 was aligned on the opposite side of the aperture, and fixed using NOA 61 which is cured by UV irradiation. SF16 (shell lenses) were manufactured by using a direct single-point diamond turning method and post-polishing. Then, drop-coating of NOA 61 was applied on BK7, and SF16 was aligned on BK7. BK7 and SF16 were fixed using NOA 61 which is cured by UV irradiation. The ledge of the aperture enabled accurate alignment between the aperture and SF16. In Figure 2.4, the surface profiles of the aperture and the SF16 were analyzed. Such profiles were characterized by using a non-contacting 3D surface profile measurement device (NH-3SPs, Mitaka Kohki).

The monocentric lens fabrication was finished by repeating the same process that is a series of assembling SF16 on the opposite side of the aperture.

2.2.2. Fabrication process and characterizations of the photodiode array.

Fabrication process of the h-SiNR-PDA started with the spin-coating of a polystyrene (PS) microsphere solution, whose diameter is 0.5 μm (Thermo Fisher Scientific), onto a silicon-on-insulator wafer, whose top silicon thickness is 1.25 μm (SOITEC). Repeated dry etching processes using reactive ion etch with oxygen gas and SF6 gas generate the silicon nanorod (SiNR) textured surface[44]. The remaining PS microspheres were eliminated by sonication and piranha solution treatment. Repeated doping processes, which are n-type doping and p-type doping, were conducted by using spin-on dopants and thermal diffusion. In detail, n-type spin-on-dopant (P509 solution; Filmtronics) was used. Then it was annealed at 200 °C for 15 min and at 975 °C for 12 min for thermal diffusion. p-type spin-on-dopant (B153 solution; Filmtronics) was used. Then it was annealed at 200 °C for 15 min and at 975 °C for 30 min for thermal diffusion. The doping profiles were characterized by using magnetic sector secondary ion mass spectrometry (IMS 7f, CAMECA; Fig. 2.5). The, the silicon nanomembrane was transfer-printed onto the polyimide (PI) bottom substrate film (Sigma Aldrich), which is spin-coated on a SiO$_2$ wafer. The silicon nanomembrane was patterned using photolithography and dry etching. Then, the Al$_2$O$_3$ layer (~25 nm) was deposited by the plasma-enhanced atomic layer deposition (ALD) and patterned using photolithography and wet etching with a buffered oxide etchant for the surface passivation. A PI film coating was conducted

for the first intermediate dielectric, whose thickness is around 1 μm. The via was patterned using photolithography and dry etching, and the deposition of first Cr/Au metal electrode and interconnection layers, whose thickness is 10/100 nm, were conducted by using the thermal evaporation and wet etching. Repeated spin-coating of the PI film for the second intermediate dielectric and repeated deposition of second Cr/Au metal electrode and interconnection layers were conducted using the same procedure. A final top PI film coating was conducted, then the overall device was patterned into a desired hexagonal mesh type array by using dry etching. The h-SiNR-PDA was then picked up from the SiO_2 wafer by using a water-soluble tape (3M Corp.), and it was transfer-printed onto a hemispherical polydimethylsiloxane mold (Dow Corning).

The individual pixel, serially connected photodiode and blocking diode in a lateral n–p–n structure, was used for electrical characterizations. A white light-emitting diode was used for the light source. For the characterization of optoelectronic device, the photocurrents of SiNR photodetectors with and without Al_2O_3 passivation, were characterized by using a parameter analyzer (B1500A, Agilent). Finally, outlier data, which are the largest and smallest experimental results, were excluded.

1. Drop-coating NOA 61

2. Aligning components

3. Fixing the components using UV curing of NOA 61

4. Filling gap between the components using NOA 61

5. Aligning and fixing another BK7 on the opposite side of the aperture

6. Drop-coating NOA 61

7. Placing the SF16 on the BK7

8. Fixing the components by UV curing of NOA 61

9. Repeating steps 7 and 8
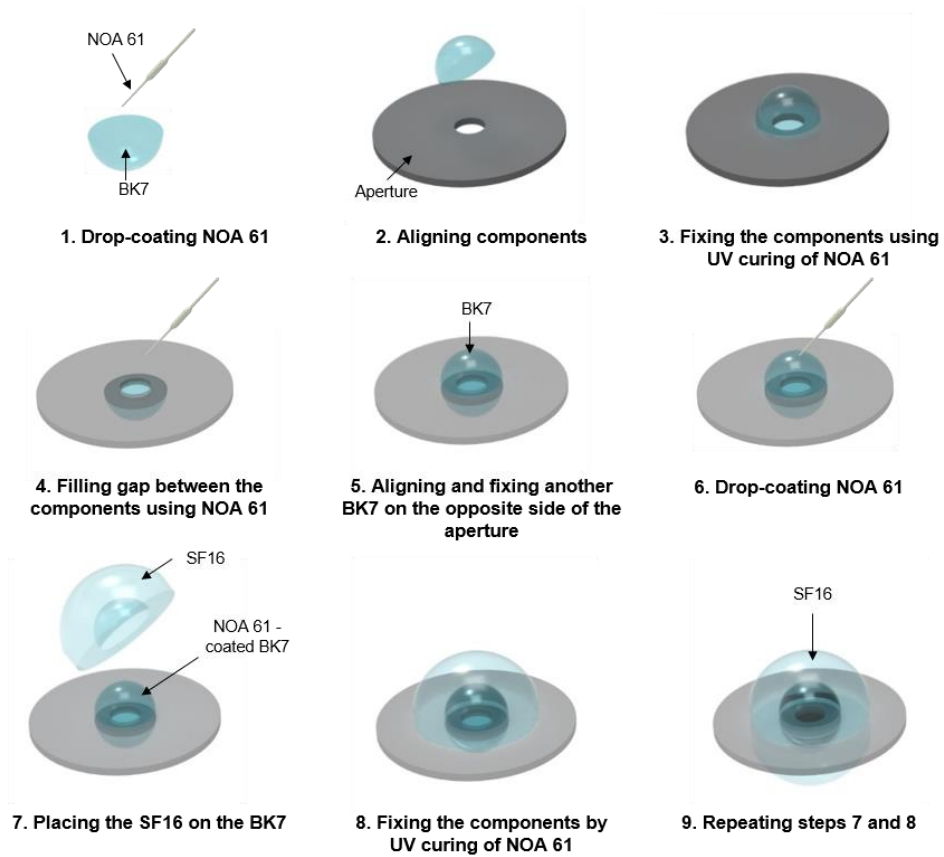
Figure 2.3. Fabrication process of the monocentric lens.

a

Ledge — 7.738 mm — Ledge

$t_{aperture}$

$2R_{aperture}$

X position (mm)

b

r = 3.806 mm,
θ = -0.1036°

Measured data
Estimated circle

Radius (mm)

r = 3.806 mm,
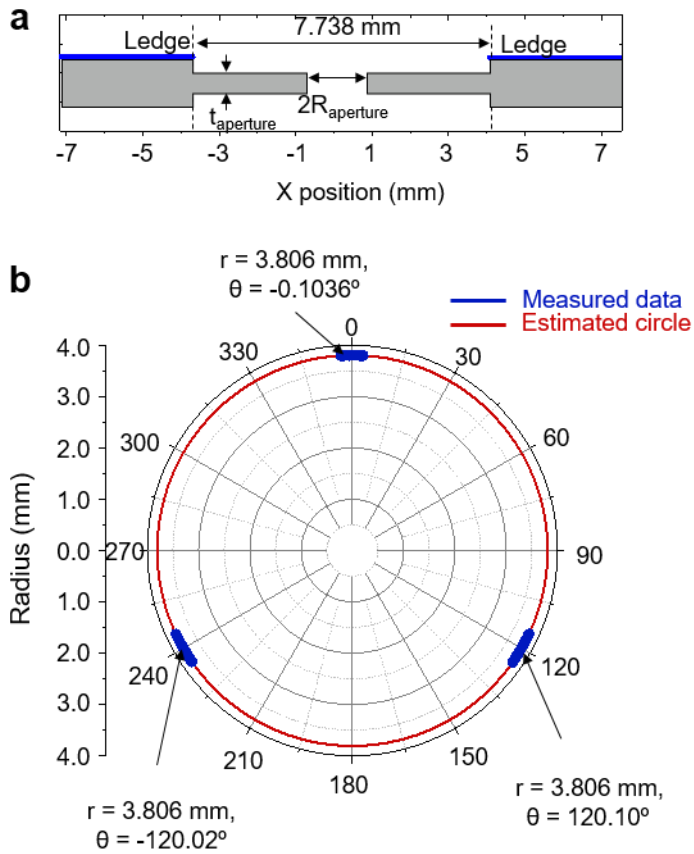θ = -120.02°

r = 3.806 mm,
θ = 120.10°

Figure 2.4. Surface profiles of the aperture (a) and the SF16 (b).
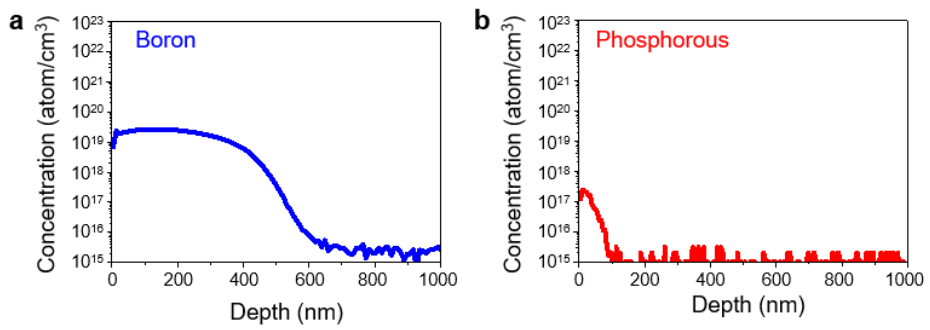
33

Figure 2.5. Doping profiles of boron (a) and phosphorous (b).

2.3 Results and discussion

2.3.1. Structural and functional advantages of the aquatic eyes

A photograph of an aquatic animal and schematic illustration of its anatomical structure are shown in Fig. 2.6. The aquatic eye has the wide visual field with high visual acuity in the dim underwater condition by virtue of a spherical lens and highly sensitive hemispherical retina[22]. Also, it has deep DoF and facile visual accommodation[20]. Such advantages support the aquatic animal to avoid enemies and to hunt for prey. If a similar method could be provided in a real world, such advantages will be useful to avoid obstacles and to track objects for a novel mobile electronics[1].

Such optical features are resulted from the structural and functional advantages of the aquatic vision which includes a monocentric lens, a hemispherical retina, and retractor and protractor muscles (Fig. 2.7). The spherical monocentric lens forms a hemispherical shaped focal plane. By matching such curved focal plane with the curved retina, the aquatic eye enables the wide visual field. Further, the parabolic RI distribution of such a lens shows minimized optical aberrations, which allows less aberrations for wide field of view imaging. The retina possesses elongated rod cells, which extend the light path to absorb more light, which is useful to sense low-intensity lights of underwater environment[22]. The retractor and protractor muscles move the lens backward and forward as a visual accommodation method.

Such a wide visual field feature is confirmed by various optical simulations. The three-dimensional ray-tracing simulation using Monte-Carlo method confirmes

the novel wide visual field imaging using the monocentric lens (Fig. 2.8a). The two-dimensional ray-tracing simulation validates less off-/on-axis aberrations of the monocentric lens.

The aquatic eye enables the deep DoF feature due to its short focal length, enabling the high-quality imaging for wide range of object distances (Fig. 2.8b). A well-focused image is acquired when the image distance (d_i) is same with the focal length (d_f) for an object placed at the object distance (d_o). All objects placed at 10 cm or farther are well-focused with $d_i = 3.55$ mm. For the closer object that is located at 2 cm, d_f becomes longer, and thus the blurred image is obtained with $d_i = 3.55$ mm. However, by changing d_i to 5.50 mm using retractor and protractor muscles, such blurred images can be re-focused well. Such a visual accommodation of the aquatic eye is simple, because it does not require the deformation of the lens (Fig. 2.9a)[21], compared to the human eye that needs to deform the lens to perform visual accommodation (Fig. 2.9b)[3].
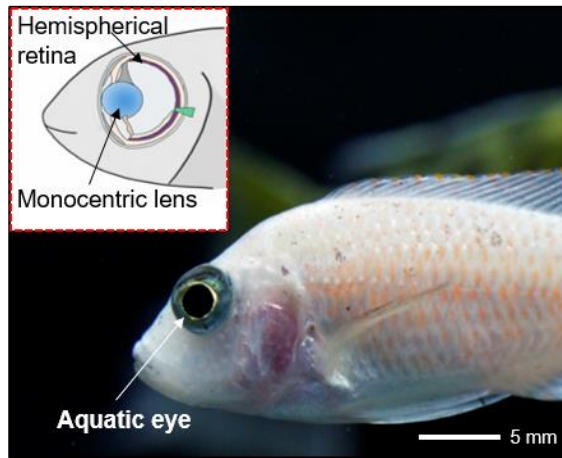
Figure 2.6. Photograph of aquatic animal and schematics of its anatomy.
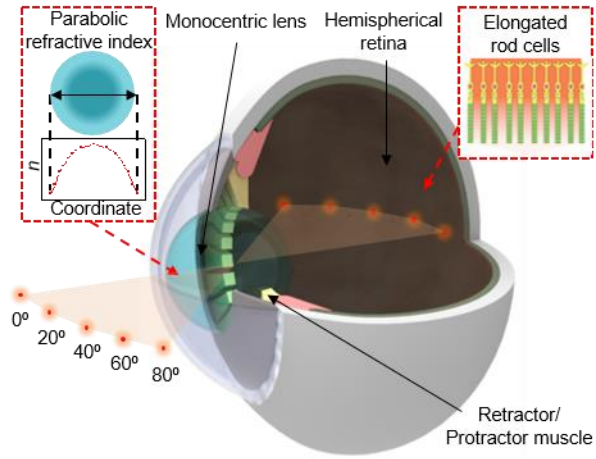
Figure 2.7. Schematic illustration of aquatic eye.
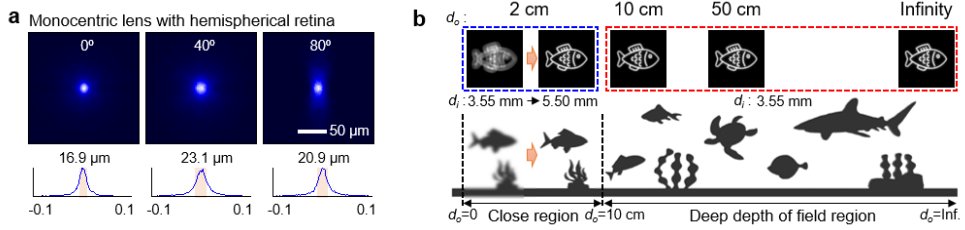
Figure 2.8. Optical simulation results of monocentric lens with hemispherical retina (a), Schematic illustration showing deep depth of field vision of aquatic vision (b).

a Visual accommodation in the aquatic vision

Distant object   Close object

Focusing by lens movement

Short focal length   Long focal length
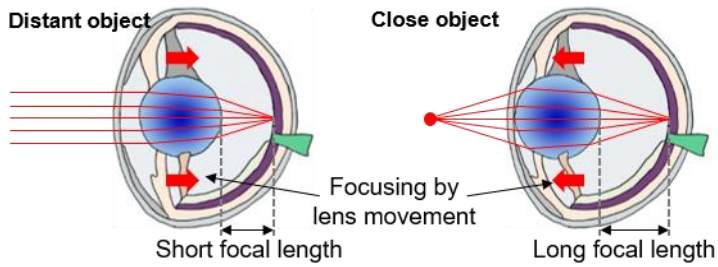
b Visual accommodation in the human vision

Distant object   Close object

Focusing by lens deformation

Figure 2.9. Schematic illustration of visual accommodation process of the aquatic vision (a), Schematic illustration of visual accommodation process of the human vision (b).

2.3.2. Monocentric lens inspired by the lens of the aquatic eyes

An artificial vision inspired by the aquatic eye can be fabricated by integrating the *mo*-lens and *h-SiNR*-PDA (Fig. 2.10a). By mimicking the monocentric lens of the aquatic eye, the fabricated *mo*-lens has a spherical structure, where BK7 and SF16 are arranged on both sides of the aperture with a NOA 61 (Fig. 2.10b). Such a symmetric shape is useful to remove the undesired wavefront error.

The monocentric lens integrated with the *h-SiNR*-PDA facilities the wide visual field imaging. Since the hemispherical structure of the *h-SiNR*-PDA is matched with its focal plane, the *mo*-lens can focus the incident lights from wide angles without off-axis aberrations, although there is an inherent attenuation of light intensity (Fig. 2.11a). Particularly, the monochromatic spot radii of the *mo*-lens are smaller than 4.2 μm for all incident angles, and such radii are much smaller than those of the conventional wide angle multi-lens or homogeneous ball lens (Fig. 2.11b). In addition, the achromatic on-/off-axis aberrations including spherical aberration (SPHA), coma aberration (COMA), and astigmati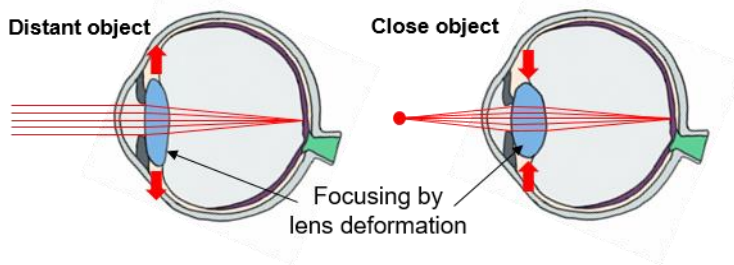sm aberration (ASTI) and the chromatic aberrations including chromatic transverse aberration (CTA) and chromatic longitudinal aberration (CLA) are smaller than those of the wide angle multi-lens or homogeneous ball lens (Fig. 2.11c)[28].

The *mo*-lens exhibits short d_f, which ranges from 2.79 mm to 5.87 mm, enabling deep DoF imaging (Fig. 2.11d). The objects, which ranges from 20 cm to infinity, shows similar d_f, which is around 2.95 mm. Therefore, such objects can be clearly focused with the same $d_{i,far} = 2.95$ mm. For the closer objects whose d_o is less than 20 cm, d_f changes, and blurred images are obtained. However, by applying the

facile accommodation method of the aquatic vision, those blurred images can be re-focused well by changing d_i.
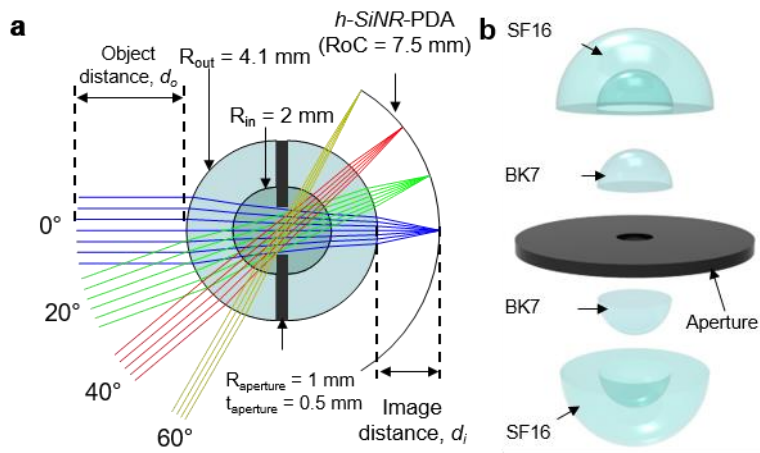
Figure 2.10. Schematic illustration of an aquatic-vision-inspired artificial vision (a), Schematic illustration of exploded view of the *mo*-lens (b).
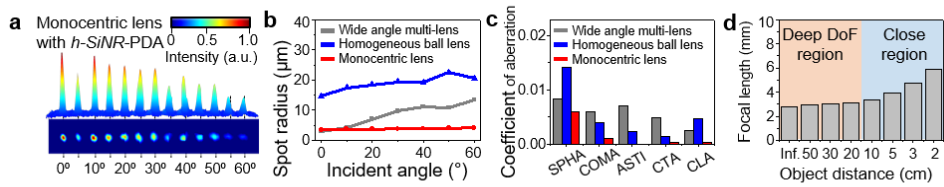
Figure 2.11. Various optical simulations of mo-lens. (a) Graph showing light intensity and size as a function of incident light angle, **(b)** Graph showing spot raidus as a function of incident light angle, **(c)** Graph showing coefficient of aberrations, **(d)** Graph showing focal length as a function of object distance.

2.3.3. Hemispherical silicon nanorod photodiode array inspired by the retina of the aquatic eyes

The *h-SiNR*-PDA was fabricated in a mesh-shape 23-by-23 hexagonal pixel array (Fig. 2.12). Individual devices are consisting of nanotextured silicon photodiode and blocking diode. The hexagonal mesh-type array design with serpentine metal interconnections minimizes the strain induced on the device[30], and the induced strain on the device is 0.02% according to finite element analysis (FEA) (Fig. 2.13). The thickness of the array is around 5.5 μm, which is useful to improve mechanical flexibility of the array[34]. Thus, *h-SiNR*-PDA could be laminated on the hemispherical surface with minimized mechanical fractures.

In the case of wide visual field imaging, the vignetting has been a serious issue to obtain clear, well focused images. Thus, the nanotexturing and surface passivation are employed to improve the light sensitivity. The textured surface passivated with a thin Al_2O_3 layer whose thickness is around ~ 25 nm, are shown in Fig. 2.14a. The transmission electron microscope (TEM) image of the nanotextured surface and a thin Al_2O_3 passivation layer is shown in Fig. 2.14b. Since the nanotextured surface decreases surface reflection and transmission[40], the nanotextured silicon device exhibits improved photo-absorption in visible wavelength, compared to the bare silicon device (Fig. 2.15). The incident lights are first diffracted on the surface of the nanorod, and then the lights are trapped inside the nanarod due to the multiple total internal reflections. Therefore, the overall incident light path is extended[40].

In addition, to the minimize the surface leakage current[41] and the charge carrier recombination[40] of the device, nanotextured surface was passivated with the Al_2O_3 thin film layer, which reduces I_{dark} and enhances I_{photo} both (Fig. 2.16). I-V characteristics curves of the nanotextured photodiode passivated with the Al_2O_3 layer, which is connected with the blocking diode in series, under various light intensities are shown in Fig. 2.17.
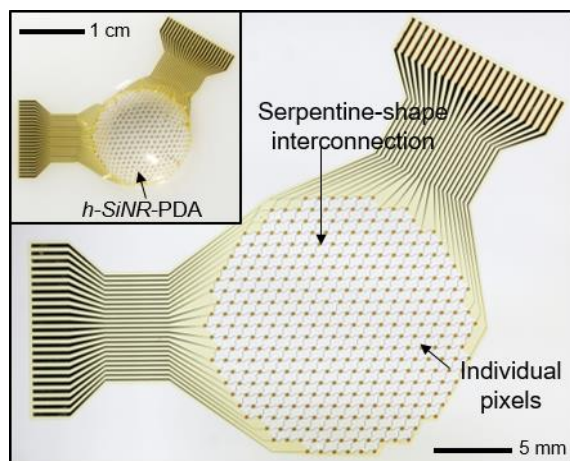
Figure 2.12. Photograph of hemispherical silicon nanorod photodiode array on the flat substrate and on the curved substrate (inset).
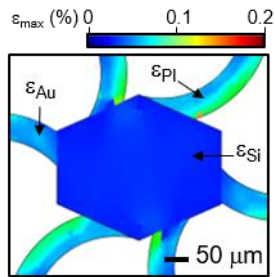
Figure 2.13. FEA results of silicon nanorod photodiode array.
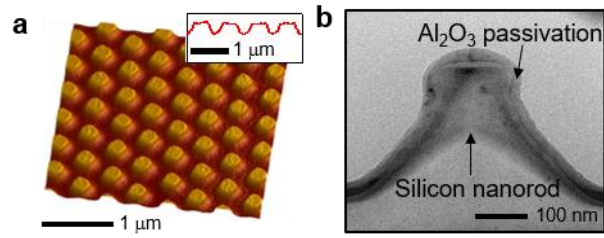
Figure 2.14. Three-dimensional AFM image of the silicon nanorod photodiode (a), Cross-sectional TEM image of the silicon nanorod photodiode (b).
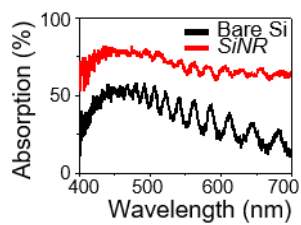
Figure 2.15. Graph showing absorption of bare silicon and silicon nanorod photodiode as a function of wavelength.
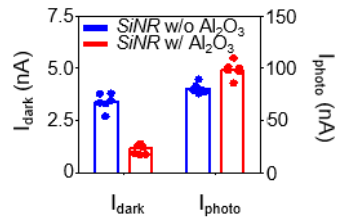
Figure 2.16. Graph showing dark current and photo current of the silicon nanorod photodiode with and without Al₂O₃ passivation.
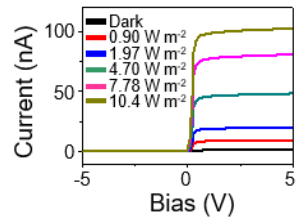
Figure 2.17. I-V characteristics curve of the silicon nanorod photodiode.

2.3.4. Various imaging demonstrations by using the aquatic vision inspired artificial vision

By Integrating the *mo*-lens, *h-SiNR*-PDA and a housing, an aquatic-vision-inspired camera module was developed (Fig. 2.18a and its inset, respectively). The aquatic-vision-inspired camera facilitates the aberration-free wide FoV imaging with the optical axis length of 11.5 mm.

The developed camera conducts various kinds of imaging demonstrations without optical aberrations. Figure 2.18b exhibits a fish-structured image captured using developed camera, and its inset shows the original object image. The developed camera also shows the deep DoF feature. Two different objects, which are a triangle ($d_{o,1}$ = 20 cm) and a square ($d_{o,2}$ = 30 cm) can be imaged well without changing $d_{i,far}$ = 2.95 mm (Fig. 2.19a). However, blurred image is obtain by using an object placed at d_o = 3 cm with $d_{i,far}$ (Fig. 2.19b). In this case, by changing the $d_{i,3cm}$ = 4.72 mm with the facile visual accommodation, well-focused/clear image can be captured.
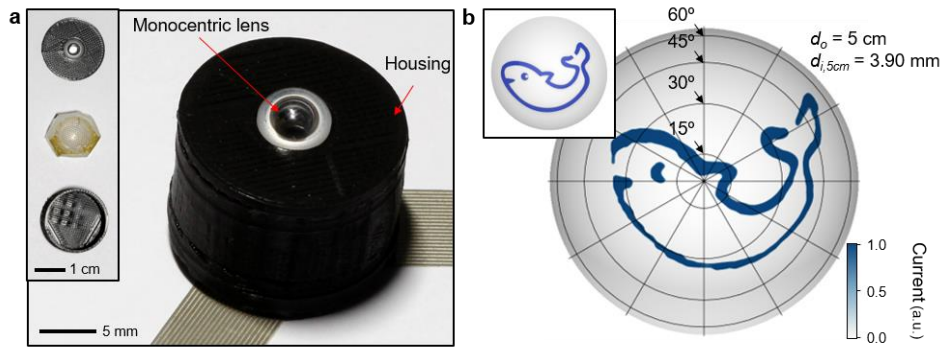
Figure 2.18. Photograph of developed bio-inspired camera (a), Imaging demonstration result showing wide visual field using such a camera (b).

a
b

$d_{o,1}$ = 20 cm
$d_{o,2}$ = 30 cm / $d_{i,far}$ = 2.95 mm d_o = 3 cm / $d_{i,far}$ = 2.95 mm d_o = 3 cm / $d_{i,3cm}$ = 4.72 mm
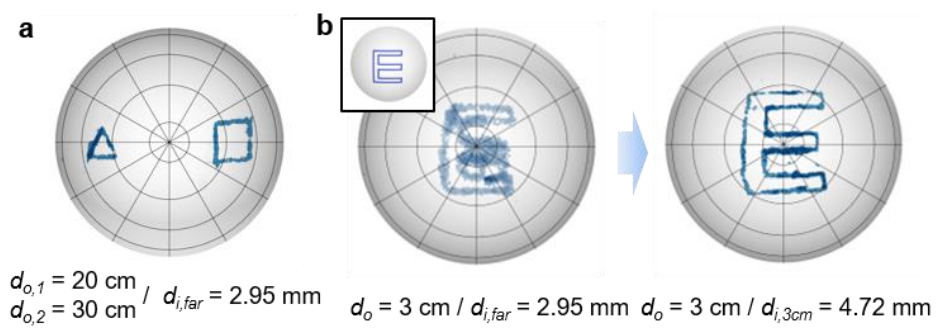
Figure 2.19. Imaging demonstration result showing deep DoF (a), and facile accommodation (b).

2.4 Conclusion

The aquatic eyes, which consists of a *mo*-lens and a highly sensitive curved retina, promotes the advancement of a next-generation miniaturized wide visual field imaging system by integrating a *mo*-lens and a h-SiNR-PDA. The distinctive features of such an aquatic-vision-inspired artificial vision are the wide visual field, miniaturized size, minimized optical aberrations, deep DoF, facile visual accommodation, and improved light sensitivity. The theoretical analyses of optical systems and imaging demonstrations using them validates all aforementioned features. The developed camera is a significant step forward in the fields of the obstacle avoidance and object tracking, providing novel approaches for the development of the next-generation mobile electronics.

2.5 Reference

* The contents of this chapter were published in Nature Electronics, 3, 546–553 (2020).

1. Floreano, D. & Wood, R. J. Science, technology and the future of small autonomous drones. *Nature* **521**, 460-466 (2015).

2. Lee, G. J., Choi, C., Kim, D.-H. & Song, Y. M. Bioinspired artificial eyes: optic components, digital cameras, and visual prostheses. *Adv. Funct. Mater.* **28**, 1705202 (2018).

3. Lee, G. J., Nam, W. I. & Song, Y. M. Robustness of an artificially tailored fisheye imaging system with a curvilinear image surface. *Opt. Laser Technol.* **96**, 50-57 (2017).

4. Zhou, F., *et al*. Optoelectronic resistive random access memory for neuromorphic vision sensors. *Nat. Nanotechnol.* **14**, 776-782 (2019).

5. Choi, C., *et al*. Human eye-inspired soft optoelectronic device using high-density MoS$_2$-graphene curved image sensor array. *Nat. Commun.* **8**, 1664 (2017).

6. Artal, P. Optics of the eye and its impact in vision: a tutorial. *Adv. Opt. Photon.* **6**, 340-367 (2014).

7. Song, Y. M., *et al*. Digital cameras with designs inspired by the arthropod eye. *Nature* **497**, 95-99 (2013).

8. Jagger, W. S. & Sands, P. J. A wide-angle gradient index optical model of the crystalline lens and eye of the rainbow trout. *Vision Res*. **36**, 2623-2639 (1996).

9. Jagger, W. S. & Sands, P. J. A wide-angle gradient index optical model of the

crystalline lens and eye of the octopus. *Vision Res*. **39**, 2841-2852 (1999).

10. Mass, A. M. & Supin, A. Y. Adaptive features of aquatic mammals' eye. *Anat. Rec.* **290**, 701-715 (2007).

11. Charman, W. N. & Tucker, J. The optical system of the goldfish eye. *Vision Res.* **13**, 1-8 (1973).

12. Ott, M. Visual accommodation in vertebrates: mechanisms, physiological response and stimuli. *J. Comp. Physiol. A* **192**, 97-111 (2006).

13. Wagner, H.-J., Frohlich, E., Negishi, K. & Collin, S. P. The eyes of deep-sea fish II. Functional morphology of the retina. *Prog. Retin. Eye Res.* **17**, 637-685 (1998).

14. Partridge, J. C., Archer, S. N. & Lythgoe, J. N. Visual pigments in the individual rods of deep-sea fishes. *J. Comp. Physiol. A* **162**, 543-550 (1988).

15. Wu, T., Hamann, S. S., Ceballos, A. C., Chang, C.-E., Solgaard, O. & Howe, R. T. Design and fabrication of silicon-tessellated structures for monocentric imagers. *Microsyst. Nanoeng.* **2**, 16019 (2016).

16. Liu, H. W., Huang, Y. & Jiang, H. Artificial eye for scotopic vision with bioinspired all-optical photosensitivity enhancer. *Proc. Natl. Acad. Sci. USA* **113**, 3982-3985 (2016)

17. Gao, M., Cho, M., Han, H.-J., Jung, Y. S. & Park, I. Palladium-decorated silicon nanomesh fabricated by nanosphere lithography for high performance, room temperature hydrogen sensing. *Small* **14**, 1703691 (2018).

18. Steel, W. H. On the choice of glasses for cemented achromatic aplanatic doublets. *Aust. J. Phys.* **7**, 244-253 (1954).

19. Sim, K., *et al.* Three-dimensional curvy electronics created using conformal additive stamp printing. *Nat. Electron.* **2**, 471-479 (2019).

20. Choi, M. K*., et al.* Wearable red-green-blue quantum dot light-emitting diode array using high-resolution intaglio transfer printing. *Nat. Commun.* **6**, 7149 (2015).

21. Savin, H*., et al.* Black silicon solar cells with interdigitated back-contacts achieve 22.1% efficiency. *Nat. Nanotechnol.* **10**, 624-628 (2015).

22. Gao, Y., *et al.* Photon-trapping microstructures enable high-speed high-efficiency silicon photodiodes. *Nat. Photonics* **11**, 301-308 (2017).

Chapter 3. Cuttlefish-eye-inspired artificial vision for high-contrast and high-acuity imaging in the shallow-water environment

3.1 Introduction

Specialized cameras for underwater robotics that can offer clear underwater images are widely used in the fields of underwater robotics[1]. Compared to the image acquisitions out of water, low signal to noise ratio (SNR) and contrast imbalance must be considered to acquire high-quality image in water environment[2]. In particular, due to the direct sunlight illumination at the shallow-water, multiple light scattering and reflection could lead to low contrast and high noise images[3]. Therefore, specialized strategies for achieving high SNR are required for the underwater image acquisition.

Cuttlefish lives in shallow-water with vertically uneven light illumination (Fig. 3.1a). To adapt to this environment, it has unique eye structure that consists of a w-shaped pupil, a single lens and curved retina with high-density belt-like photoreceptor region and polarization sensitive photoreceptors (Fig. 3.1b)[3-5]. Distinctive w-shaped pupil enables to balance out vertically uneven light illumination. The high-density belt-like photoreceptor region placed in horizontal direction enables high visual acuity near the horizon[4]. Also, polarization sensitive photoreceptors of cuttlefish can efficiently break and recognize camouflaged preys,

enabling even higher visual acuity[5]. These strategies for realizing high-contrast-sensitivity that cuttlefish use have promoted the development of high-contrast camera specialized for shallow-water environment.

Here, we report a cuttlefish-eye-inspired high-contrast and high-acuity camera that specializes in the low-contrast shallow-water environment. By mimicking the unique w-shaped pupil structure of cuttlefish-eye, a cuttlefish-eye-inspired camera compensates uneven vertical light distribution by blocking ~20% of the direct sunlight above its optical axis, compared to the circular pupil. In addition, the cylindrical silicon photodiode array (c-Si-PDA) which contains high-density belt-like pixels allows to have wide horizontal-field-of-view (~120º) with high-resolution inspired by curved retina of cuttlefish-eye. The flexible, linear polarizing film on top of the c-Si-PDA maintains the average degree of polarization of 80% in visible regions, which could enable high-contrast polarization imaging.
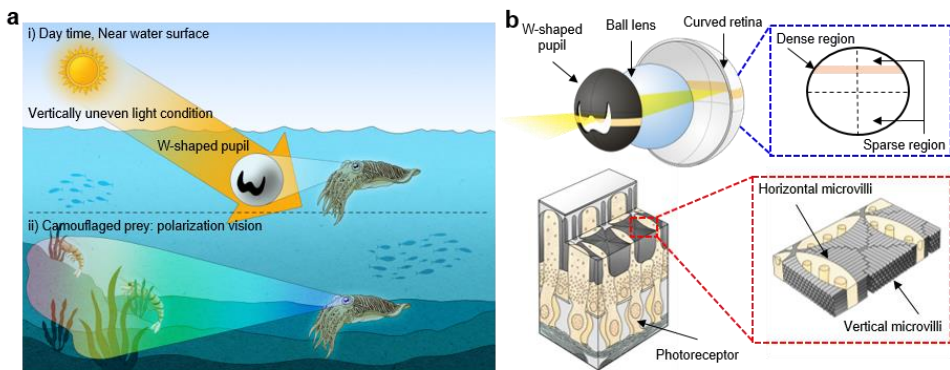
Figure 3.1 Schematic illustration of shallow-water environment (a), schematic illustration of anatomy of cuttlefish-eye (b).

3.2 Experimental Section

3.2.1. Fabrication of flexible/laminatable polarizing film

Drop-casting of single-wall carbon nanotubes (SWCNTs) and P(VDF-TrFE-CFE) as a stretchable polymer on a glass substrate and subsequent evaporation process are used for fabricating flexible and laminatable polarization film (FLPF).

3.2.2. Fabrication cylindrical image sensor array and characterization

Fabrication process (Fig. 3.2) of the cylindrical image sensor array started with the repeated doping procedures, n-type doping and p-type doping with thermal diffusion method. In detail, n-type spin-on-dopant (P509 solution; Filmtronics) was used. Then it was annealed at 200 °C for 15 min and at 975 °C for 12 min for thermal diffusion. p-type spin-on-dopant (B153 solution; Filmtronics) was used. Then it was annealed at 200 °C for 15 min and at 975 °C for 30 min for thermal diffusion. Then, the silicon nanomembrane was transfer-printed onto the polyimide (PI) bottom substrate film (Sigma Aldrich), which is spin-coated on a SiO_2 wafer. The silicon nanomembrane was patterned using photolithography and dry etching. A PI film coating was conducted as an intermediate dielectric (thickness of 1 μm). The via was patterned using photolithography and dry etching, and the deposition of Cr/Au metal electrode and interconnection layers (thickness of 10/100 nm), were conducted by using the thermal evaporation and wet etching. Repeated spin-coating of the PI film for the intermediate dielectric and repeated deposition of Cr/Au metal electrode and interconnection layers were performed using the same procedure. A final top PI film coating was performed, then the overall device was patterned into a desired form by using dry etching. The cylindrical photodiode array was then picked up from the SiO_2 wafer by using a water-soluble tape (3M Corp.), and it was transfer-printed onto a cylindrical polydimethylsiloxane mold (Dow Corning). The individual pixel, serially connected photodiode and blocking diode in a lateral n–p–n structure, was used for electrical characterizations. A white light-emitting diode was used as a light source.

1. n/p-doping   2. Transfer-printing of device   3. Patterning of device

4. 1st metal electrode deposition   5. 2nd metal electrode deposition   6. Patterning of overall device layer

7. Picking-up of the device using water-soluble tape   8. Transfer-printing of the device   9. Transfer-printing of the polarization film
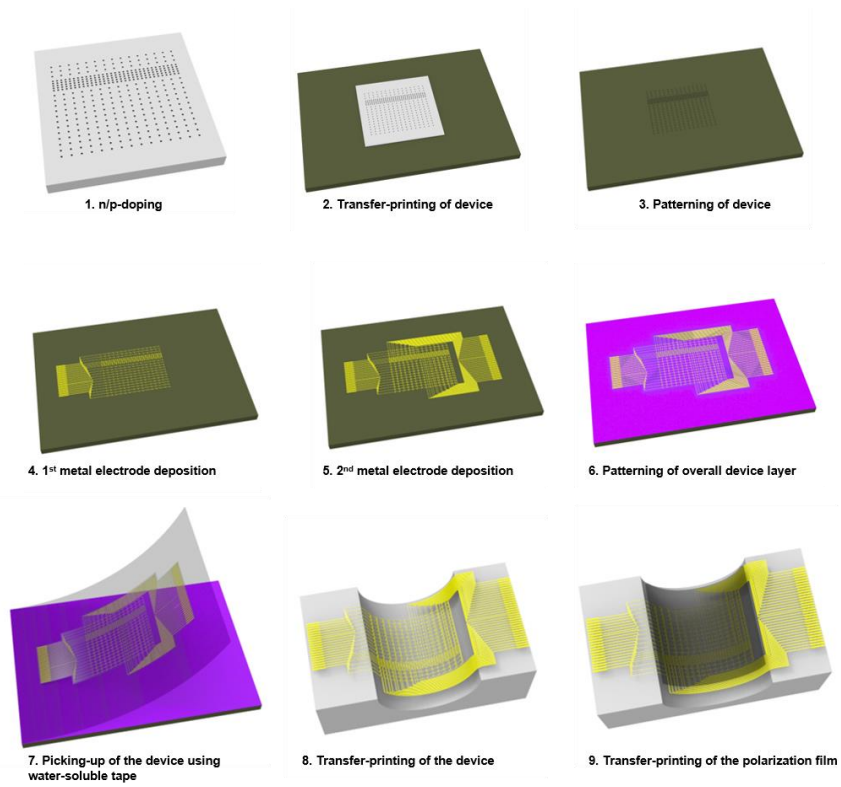
Figure 3.2. Schematic illustration showing fabrication process of cylindrical silicon photodiode array.

3.3 Results and discussion

3.3.1. Optical simulations

A cuttlefish-vision-inspired artificial imaging system is systematically designed using 3D ray-tracing simulations (Fig. 3.3a). An exploded view of fabricated lens and aperture, that consist of W-shaped aperture, two BK7 half-ball lenses, and center aperture is shown in Fig. 3.3b. The circular aperture is used for the comparison. The horizontal focusing capabilities of circular aperture and W-shaped aperture are characterized by comparing their spot radii as a function of horizontal incident angles (Fig. 3.4). Spot radii of the imaging system with W-shaped aperture shows smaller than that with circular aperture in all angles (Fig. 3.4). In particular, spot radii of the imaging system with W-shaped aperture decrease as the incident angle increases due to the reduced coma aberrations at the periphery of the W-shaped aperture because it serves as a vertical pupil.

a

−35°
−17.5°
0°
17.5°
35°

f = 1.606 mm

Cylindrical image plane

5 mm

b

W-shaped pupil
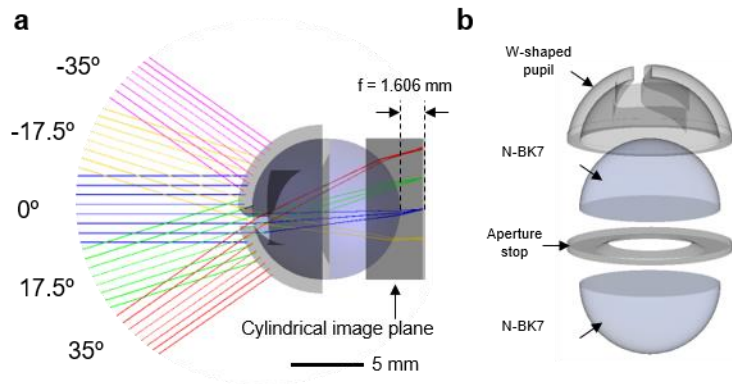
N-BK7

Aperture stop

N-BK7

Figure 3.3. Schematic illustration showing the integrated lens system (a), exploded view of the integrated lens system.
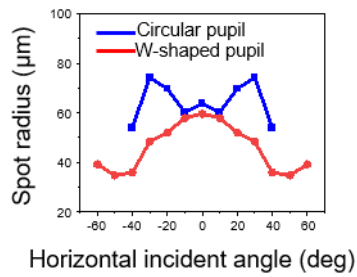
Figure 3.4. Graph showing spot radii of circular pupil and W-shaped pupil as a function of horizontal incident angle.

3.3.2. Characterization and integration of the cylindrical silicon photodiode array

Inspired by the belt-like photoreceptor distribution of cuttlefish, the cylindrical silicon photodiode array is fabricated (Fig. 3.5a). The array has high-density area, which is slightly above the center line, and the rest region of the array is low-density area. Then, the device is transfer-printed onto the cylindrical-shaped PDMS mold without mechanical fracture due to the ultrathin device structure (Fig. 3.5b). Finally, the fabricated polarization film is transfer-printed on the cylindrical silicon image sensor array without mechanical fracture due to its high flexibility (Fig. 3.5c).

The electrical characterization of fabricated optoelectronic device is performed. I-V curves of the optoelectronic device without polarization filter under various light intensities are shown in Fig. 3.6a. In addition, I-V curves of the optoelectronic device with polarization filter under two different kinds of polarized lights are also shown in Fig. 3.6b. The light parallel to the polarized direction of film is absorbed by the CNT-based polarization film. Thus, the photocurrent of the optoelectronic device with polarization filter under the light illumination which is polarized parallel to the polarized direction of film, is measured to be ~ 10 nA. Such a photocurrent is almost negligible compared to photocurrent of the optoelectronic device (~ 74 nA) with polarization filter under the light illumination which is polarized perpendicular to the polarized direction of film. Both photocurrents are measured at the bias voltage of 4 V. Such I-V curves indicate that the developed

optoelectronic devices can be further applied to the high-contrast polarization imaging.

All the fabricated optical components, that consist of aperture, lens and image sensor array, are integrated (Fig. 3.7). Such an integrated optical system could be applied to various imaging demonstrations, such as wide horizontal visual field imaging and high-contrast polarization imaging.
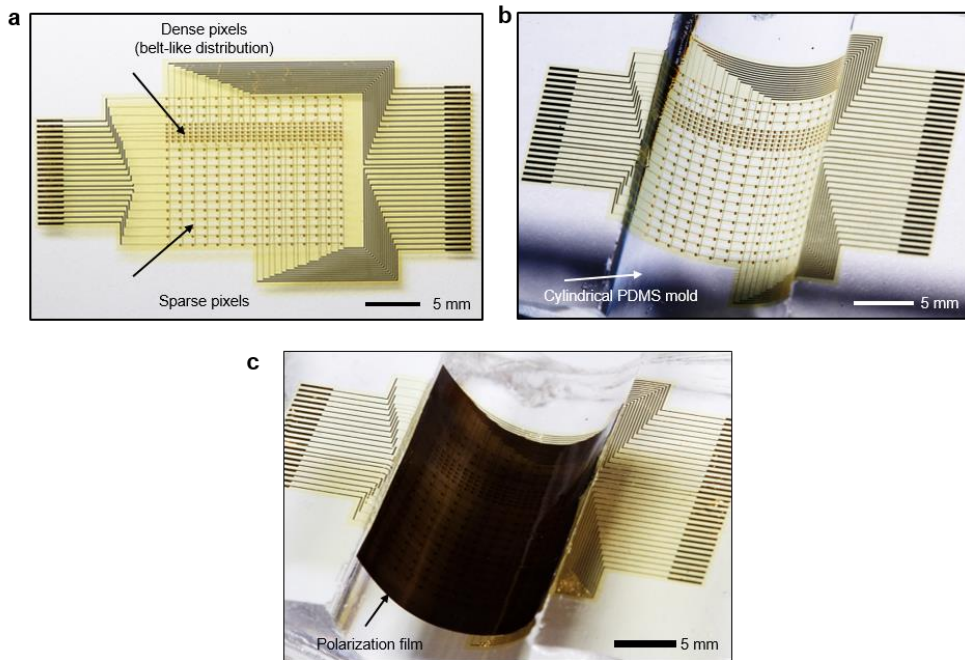
Figure 3.5. Photograph of silicon photodiode array. (a) Silicon photodiode array that is transfer-printed on the flat substrate, **(b)** Silicon photodiode array that is transfer-printed on the cylindrical PDMS mold without polarization filter. **(c)** Silicon photodiode array that is transfer-printed on the cylindrical PDMS mold with polarization filter.

Figure 3.6. I-V curves. (a) I-V curves of silicon photodiode array without polarization filter under various light intensities, **(b)** I-V curves of silicon photodiode array with polarization filter under various polarized light illuminations.
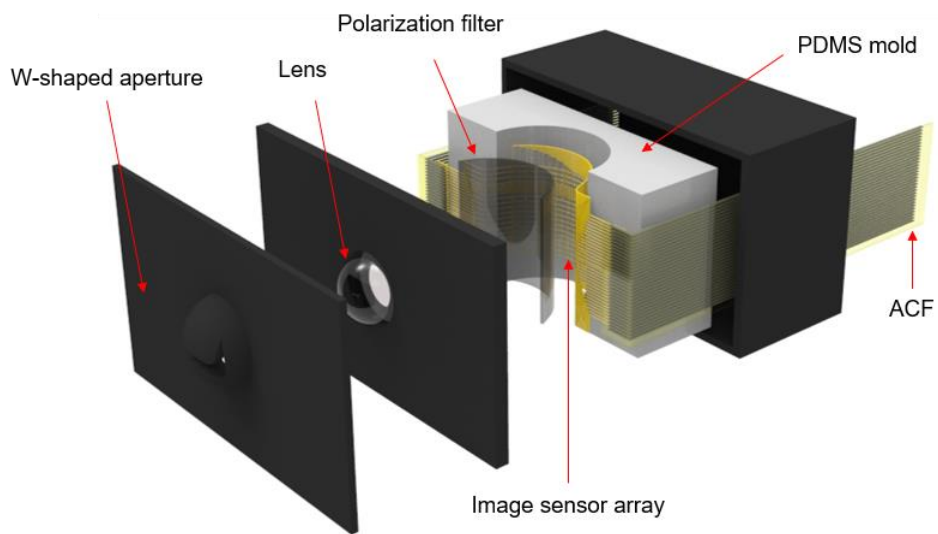
Figure 3.7. Schematic illustration of the overall optical system.

3.4 Conclusion

High-quality shallow-water imaging systems are of use in developing surveillance, navigation and monitoring systems in underwater environment. Balancing uneven vertical light distribution and improving signal-to-noise ratio in shal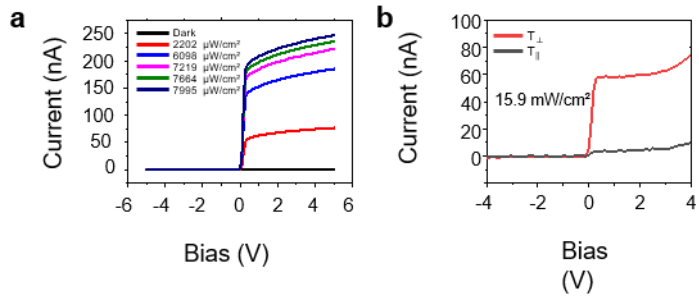low-water environment are key to develop such specialized cameras. The eye of cuttlefish, consisting of a w-shaped pupil, a single lens and curved retina with high-density belt-like photoreceptor region and polarization sensitive photoreceptors, could be of a good inspiration for developing high-quality shallow-water imaging systems. We report a cuttlefish-eye-inspired artificial vision consisting of a w-shaped aperture, a single ball-lens, a flexible polarizing film and a cylindrical silicon photodiode array with high-density pixel region. Furthermore, the developed imaging system could enable a wide horizontal-field-of-view with high-resolution and a high-contrast polarization imaging.

3.5 Reference

1. Lu, H., Li, Y., Zhang, L. & Serikawa, S. Contrast enhancement for images in turbid water. *J. Opt. Soc. Am. A* **32**, 886 (2015).

2. Fei, L. & Yingying, W. The research of underwater image de-noising method based on adaptive wavelet transform. in The 26th Chinese Control and Decision Conference (2014 CCDC) 2521–2525 (IEEE, 2014).

3. Mäthger, L. M., Hanlon, R. T., Håkansson, J. & Nilsson, D.-E. The W-shaped pupil in cuttlefish (Sepia officinalis): functions for improving horizontal vision. *Vision Res.* **83**, 19–24 (2013).

4. Watanuki, N., Kawamura, G., Kaneuchi, S. & Iwashita, T. Role of vision in behavior, visual field, and visual acuity of cuttlefish Sepia esculenta. *Fish. Sci.* **66**, 417–423 (2000).

5. Talbot, C. M. & Marshall, J. N. The retinal topography of three species of coleoid cephalopod: significance for perception of polarized light. *Philos. Trans. R. Soc. B Biol. Sci.* **366**, 724–733 (2011).

Chapter 4. Curved neuromorphic image sensor array using a MoS₂-organic heterostructure inspired by the human visual recognition system

4.1 Introduction

Recent progresses in the image recognition systems have facilitated image-data-based processing applications[1]. Such efficient image recognition processes are necessary for various machine vision tasks[2]. However, image recognition using current imaging system and image data processors, is unsuitable for efficient and low energy consumption systems[3] since current systems perform object recognition using massive data storage, processing, chip-to-chip communications[4] aberration-free imaging, and bulky optics[5]. In the case of visual recognition system of human, visual information is acquired by a single lens, hemispherical retina, and brain. And then, recognition process is conducted by using neural network in the visual cortex[1]. Therefore, such visual recognition process of human could outperform the conventional systems in terms of efficiency[1].

Inspired by the human's neural network, memristor crossbar arrays have been developed. Such memristor crossbar arrays could efficiently conduct vector matrix multiplications by applying the neural network in hardware[6]. In terms of optics, human eye inspired system that consists of a curved image sensor arrays and a single lens has been developed[7]. However, with those systems, novel image recognition

devices that can perform energy efficient image recognition with a simple optics at the same time cannot be realized.

Here, we report a curved neuromorphic image sensor array (cNISA) based on MoS$_2$ and poly(1,3,5-trimethyl-1,3,5-trivinyl cyclotrisiloxane) (pV3D3) heterostructure for high-quality imaging and energy-efficient pre-processing of image information with a single device. The cNISA consists of a plano-convex lens and a curved image sensor array, and can realize novel imaging capability and photon-triggered synaptic plasticity. Without complicated optical components and a series of storage, processing, and communications of image data, a pre-processed image from noisy image inputs could be successfully obtained.

4.2 Experimental Section

4.2.1. Synthesis of graphene using chemical vapor deposition.

After annealing of a copper foil (Alfa Aesar, USA) for 30 min at the temperature of 1000 °C with a gas flow of H_2 (8 sccm, 0.08 Torr), additional gas flow of CH_4 (20 sccm, 1.6 torr) was applied for 20 min at the temperature of 1000 °C. Then, temperature of the chamber was changed to room temperature under a gas flow of H_2 (8 sccm, 0.08 Torr).

4.2.2. Synthesis of MoS_2 using chemical vapor deposition.

Sulfur (0.1 g; Alfa Aesar, USA) and MoO_3 (0.3 g; Sigma Aldrich, USA) were placed at the upstream and center of the chamber, respectively. A piranha solution and O_2 plasma-treated SiO_2 wafer was placed at the downstream of the MoO_3. After annealing at the temperature of 150 °C for 30 min under a gas flow of Ar (50 sccm, 10 torr), the temperature of the chamber was changed up to 650 °C for 20 min and was maintained at the temperature of 650 °C for 5 min under a gas flow of Ar (50 sccm, 10 torr). The temperature of sulfur was maintained at 160 °C. After those processes, the temperature of the chamber was changed to room temperature under a gas flow of Ar (50 sccm, 10 torr).

4.2.3. Deposition of pV3D3 using initiated chemical vapor deposition

The device was placed in the iCVD chamber at the temperature of 50 °C. The temperature of the filament was maintained at 140 °C. 1,3,5-trimethyl-1,3,5-trivinyl cyclotrisiloxane (V3D3, 95%; Gelest, USA) and di-tert-butyl peroxide (TBPO, 97%;

Sigma Aldrich, USA) were vaporized and flowed inside the chamber during the deposition process. The ratio of V3D3 and TBPO was maintained as 2:1, and the pressure of the chamber was controlled to be 0.3 Torr.

4.2.4. Fabrication process of cNISA

First, a polyimide (PI) film (Sigma Aldrich, USA) was spin-coated on a SiO_2 wafer. Then, a Si_3N_4 film deposition (~15 nm thickness) was conducted using plasma-enhanced CVD. And the Si_3N_4 thin film was patterned using photolithography and dry etching. CVD grown graphene for an electrode material was transfer-printed onto Si_3N_4, and was patterned for the source/drain electrodes. Ti/Au layers, whose thickness is around 5 nm/25 nm, were deposited. CVD grown-MoS_2 layer for the light-sensitive channel was transfer-printed onto the graphene electrodes. And the MoS_2 layer was patterned using photolithography and dry etching. A pV3D3 layer, whose thickness is around 25 nm, was deposited by iCVD for the dielectric layer. Then it was patterned using photolithography and dry etching. The Ti/Au layers, whose thickness is around 5 nm/25 nm, was deposited for the gate electrode by thermal evaporation, and patterned using a lift-off process. Additional Ti/Au layers, whose thickness is around 5 nm/25 nm, were deposited and patterned for ACF pad metal. At last, a parylene film, whose thickness is around 1 μm thickness, was deposited for the top encapsulation and was dry-etched. The fabricated device was picked-up from the SiO_2 wafer with a water-soluble tape (3M Corp., USA), and then transfer-printed onto a hemispherical mold that is fabricated with the polydimethylsiloxane (PDMS; Dow Corning, USA).

4.2.5. Electrical characterization of optoelectronic devices

The electrical properties of Al_2O_3-PTr as a control device and pV3D3-PTr were measured with a parameter analyzer (B1500A, Agilent, USA). A white light-emitting diode was applied as a light source. The optical input pulses with 0.5 sec time intervals were generated by using the Arduino UNO.

4.2.6. Characterization of heterostructure of MoS_2 and pV3D3

The surface potentials of a heterostructure of a MoS_2 and Al_2O_3 as a control device, and MoS_2 and pV3D3 were measured by using the Kelvin probe force microscope (Dimension Icon, Bruker, USA). Raman spectra and photoluminescence (PL) spectra of the CVD grown MoS_2 and heterostructure of MoS_2 and pV3D3, and MoS_2 and Al_2O_3 were measured by using Raman/PL micro-spectroscopy (Renishaw, Japan) with 532 nm laser.

4.2.7. Imaging demonstration using developed device

The programmed optical input pulses with 0.5 sec time interval were introduced to the device. The current amplifiers, that are transimpedance amplifiers and inverters, and power supplying chips were added on a printed circuit board (PCB). Individual pixels in the array are connected to the current amplifier using ACF.

4.3 Results and discussion

4.3.1. Curved neuromorphic image sensor array (cNISA) and single lens optics

The human eye exhibits very simple optics compared to the conventional optics in terms of the number of lenses it needs. Also, high-quality aberration free imaging could be obtained with such systems due in large to the hemispherical retina which perfectly matches with the focal plane formed by the single lens[5,8] (Fig. 4.1a). The human neural network shows highly efficient unstructured data classifications based on the synaptic plasticity that includes short-term plasticity (STP) and long-term potentiation (LTP)[9].

Inspired by aforementioned features of human vision system, the curved neuromorphic image sensor array with a plano-convex lens was developed. Such imaging system can detect optical inputs and convert them into pre-processed outputs (Fig. 4.1b). These optoelectrical responses are induced by the photon, and such phenomena are similar to the synaptic plasticity of the neural network. The cNISA could efficiently acquire image data, and derive weighted electrical outputs due to the heterostructure of MoS_2 and pV3D3 at the same time in a single device.

The photocurrents of pixel, which receives frequent optical inputs, gradually increase according to the number of optical inputs (LTP; retention time of 3600 sec using 20 optical pulses). And photocurrents of pixel, which receives infrequent optical inputs, rapidly decrease (STP; retention time of 1200 sec using a single optical pulse). Such electrical outputs of pixels are the weighted value optical inputs, that reflect the history of induced optical inputs. By measuring the electrical outputs

of our cNISA, a pre-processed image outputs can be obtained, which does not need massive image data storage, communications, and processing steps.
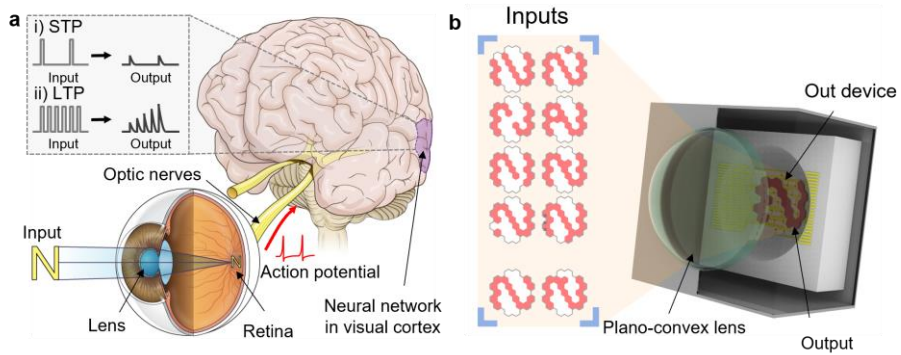
Figure 4.1. Schematic illustrations showing human visual recognition system (a), the developed curved neuromorphic imaging system that consists of a plano-convex lens and cNISA (b).

4.3.2. Photon-triggered synaptic plasticity of the device

The photon-triggered synaptic plasticity of the heterostructure of MoS_2-pV3D3 phototransistor (pV3D3-PTr) is characterized and analyzed. As explained in the experiment sections, the pV3D3-PTr are fabricated with a Si_3N_4 as a substrate, graphene as source/drain electrodes, a MoS_2 as a light-sensitive material, a pV3D3 as a dielectric layer, and a Ti/Au metal as a gate electrode (Fig. 4.2a). An optical microscope image (Fig. 4.2b) and cross-sectional transmission electron microscope (TEM) images (Fig. 4.2c) are shown.

The photo-response of pV3D3-PTr shows the synaptic plasticity that includes the rapid decay of photocurrents under infrequent optical inputs (Fig. 4.3a; STP) and the accumulation of photocurrents under frequent optical inputs (Fig. 4.3b; LTP). The accumulation of photocurrents is larger according to the amount of applied optical inputs in the case of LTP. Such photon-triggered optoelectrical responses are due to the two major features which include quasi-linear time-dependent photocurrent generation and prolonged photocurrent decay.

The quasi-linear time-dependent photocurrent generation of our pV3D3-PTr are characterized (Fig. 4.4 top). As a comparison group, a control device which consists of a MoS_2-Al_2O_3 phototransistor (Al_2O_3-PTr) was fabricated. The control device of Al_2O_3-PTr exhibits a non-linear time-dependent photocurrent generation as shown in Fig. 4.4 bottom. Also, linearity factors (α), that mean a degree of linearity of the photocurrent according to the illumination time, are analyzed, which are α_{pV3D3} of 1.52 and α_{Al2O3} of 2.50. Thus, pV3D3-PTr exhibits a more linear feature than the control device.

84

The prolonged photocurrent decay of pV3D3-PTr is characterized (Fig. 4.5a). The pV3D3-PTr's decay time constant (τ_{decay}), that means the time it takes to fall to the 1/e of original level, depends on the number of optical inputs, which are $\tau_{decay,LTP}$ of 8.61 sec and $\tau_{decay,STP}$ of 1.43 sec. The synaptic weight (A_n/A_1), that indicates a ratio of the photocurrent formed by n optical pulses to the photocurrent formed by 1 optical pulse, is shown in Fig 4.5b. While A_n/A_1 of pV3D3-PTr ($A_{25}/A_1 \sim 5.93$) gradually increases as a function of the number of optical pulses, A_n/A_1 of the control device ($A_{25}/A_1 \sim 2.89$) is almost saturated after five optical pulses, showing a large difference between them.
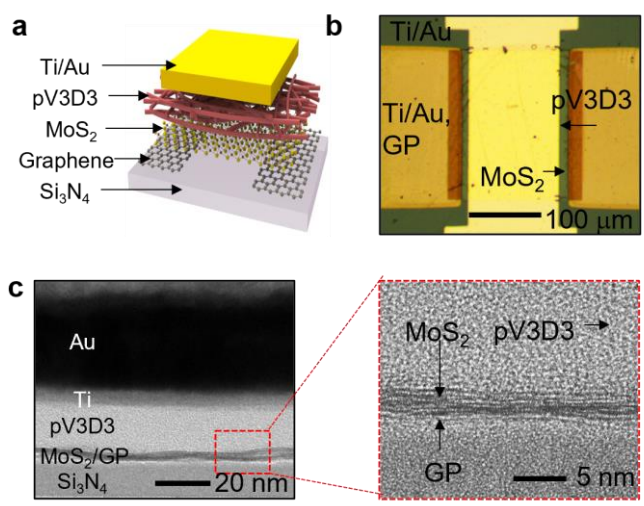
Figure 4.2. Schematic illustration showing individual pixel of cNISA (a), optical microscope image of individual pixel of cNISA (b), TEM image individual pixel of cNISA (c).
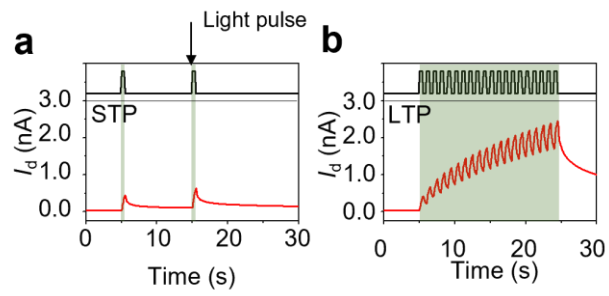
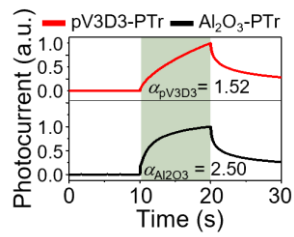**Figure 4.3. Graphs showing photocurrent of cNISA as a function of time.** STP **(a)**, LTP **(b)**.

Figure 4.4. Graph showing photocurrent (a.u.) as a function of time. pV3D3-PTr (top), Al$_2$O$_3$-PTr **(bottom).**
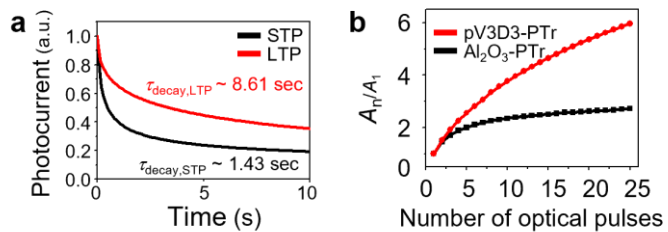
Figure 4.5. Graph showing photocurrent (a.u.) as a function of time (a), graph showing A_n/A_1 as a function of the number of optical pulses (b).

4.3.3. Imaging demonstration for a pre-processed image acquisition using the device

The fabricated cNISA, whose array size is 31 pixels, and a plano-convex optics is then integrated to obtain a pre-processed image of various patterns of input signals (Fig. 4.6a). The explode view of overall system is shown in Fig. 4.6b. The pixels in cNISA are distributed regularly, and by using ultrathin materials and intrinsically soft materials, such as MoS_2, graphene, pV3D3 and PI encapsulation, the array shows sufficient flexibility. Thus, the array could be successfully transfer-printed onto the curved surface with minimized mechanical strain (Fig. 4.7). The induced strain of the curved image sensor array on the curved surface was shown to be smaller than 0.053 % (Fig. 4.8).

The acquisition of images and then deriving of a pre-processed output images are conducted by using the developed system (Fig. 4.9). First, noisy C-shaped optical inputs, that consist of 20 optical pulses with 0.5 sec durations and 0.5 sec intervals, are induced to the cNISA. In response to the frequent optical signals, a large amount of photocurrent is accumulated in the corresponding pixels. In addition, in response to the infrequent optical signals, a photocurrent is rapidly decreased in the corresponding pixels. Finally, a pre-processed C-shaped output image is obtained, and the C-shaped image was maintained for around 30 seconds. After such processes, the remaining image, which is an afterimage, can be clearly eliminated by inducing a positive gate bias of 1 V. Therefore, photocurrents of all the pixels were return to the initial state. Then, another patterned image input is irradiated to the cNISA once more. A pre-processed N-shaped output image is successfully obtained from noisy

N-shaped optical inputs, that consist of 20 optical pulses with 0.5 sec durations and 0.5 sec intervals. By using an integrated single neuromorphic imaging device, a neuromorphic imaging demonstration was successfully demonstrated with a single measurement.
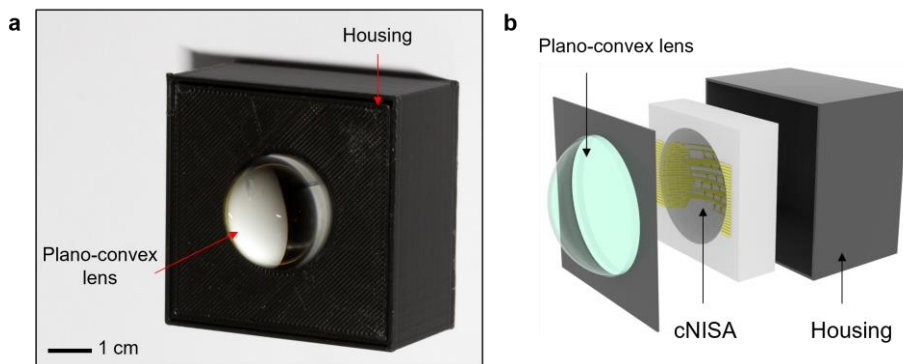
Figure 4.6. Photograph of integrated system that consists of cNISA, plano-convex lens, mold, and housing (a), schematic illustration of exploded view of overall system (b).
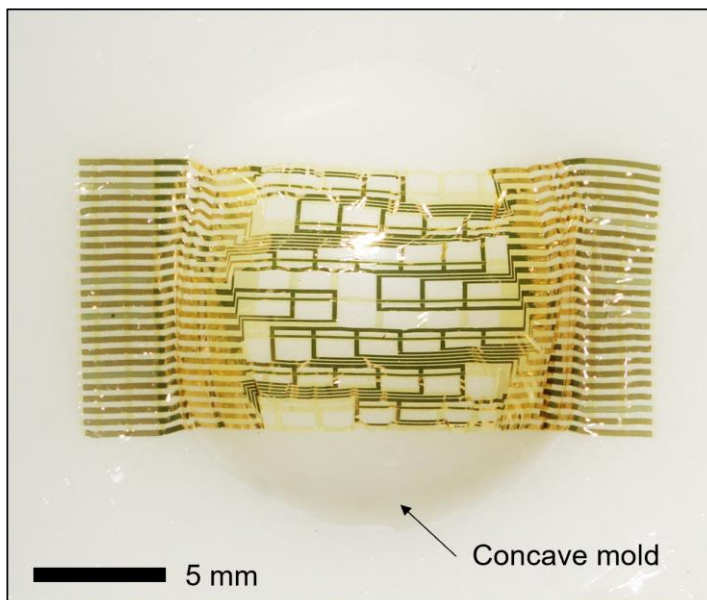
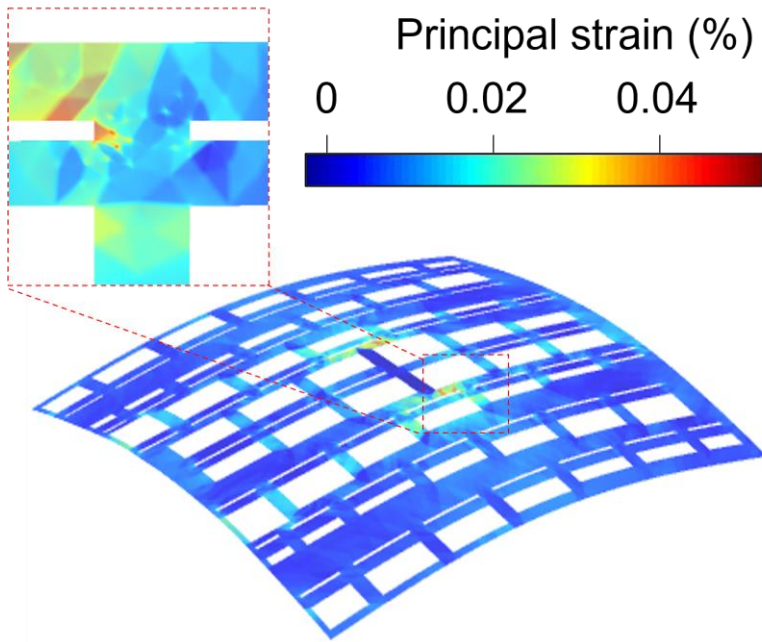**Figure 4.7. Photograph of the cNISA transfer-printed on the hemispherical PDMS mold.**

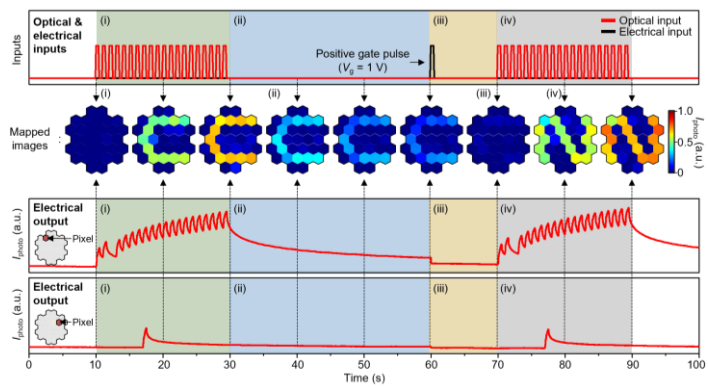**Figure 4.8. Simulation results for first principal strain distribution.**

Figure 4.9. Neuromorphic imaging demonstration results using the cNISA.

4.4 Conclusion

In this paper, inspired by the unique advantages of the human visual recognition system, that includes a single lens, curved retina, and efficient image data processing, we reported a curved neuromorphic image sensor array based on using a heterostructure of MoS_2 and pV3D3. The pV3D3-PTr exhibited quasi-linear time-dependent photocurrent generation and prolonged photocurrent decay, facilitating the photon-triggered synaptic plasticity which is experimentally and theoretically analyzed. With the use of developed device and imaging demonstration set-up, a pre-processed image output was successfully obtained using programmed optical inputs. Additional strategies for achieving high photosensitivity can improve the signal to noise ratio of the device, further. The developed system can enhance the image recognition efficiency, and can be applied to the recently developed novel machine vision devices[10,11].

4.5 Reference

1. Zhou, F. et al. Optoelectronic resistive random access memory for neuromorphic vision sensors. *Nat. Nanotechnol.* **14**, 776-782 (2019).

2. Roy, K., Jaiswal, A. & Panda, P. Towards spike-based machine intelligence with neuromorphic computing. *Nature* **575**, 607-617 (2019).

3. Zidan, M. A., Strachan, J. P. & Lu, W. D. The future of electronics based on memristive systems. *Nat. Electron.* **1**, 22-29 (2018).

4. Jeong, D. S. & Hwang, C. S. Nonvolatile memory materials for neuromorphic intelligent machines. *Adv. Mater.* **30**, 1704729 (2018).

5. Choi, C. et al. Human eye-inspired soft optoelectronic device using high-density MoS_2-graphene curved image sensor array. *Nat. Commun.* **8**, 1664 (2017).

6. Sheridan, P. M. et al. Sparse coding with memristor networks. *Nat. Nanotechnol.* **12**, 784-789 (2017).

7. Lee, W. et al. Two-dimensional materials in functional three-dimensional architectures with applications in photodetection and imaging. *Nat. Commun.* **9**, 1417 (2018).

8. Jung, I. et al. Dynamically tunable hemispherical electronic eye camera system with adjustable zoom capability. *Proc. Natl. Acad. Sci. USA* **108**, 1788-1793 (2011).

9. Lee, M. et al. Brain-inspired photonic neuromorphic devices using

photodynamic amorphous oxide semiconductors and their persistent photoconductivity. *Adv. Mater.* **29**, 1700951 (2017).

10. Mennel, L. et al. Ultrafast machine vision with 2D material neural network image sensors. *Nature* **579**, 62–66 (2020).

11. Jang, H. et al. An atomically thin optoelectronic machine vision processor. *Adv. Mater.* **32**, 2002431 (2020).

요약 (국문초록)

생체모방 인공 시각 및 뉴로몰픽 이미징 디바이스

학번: 2016-20992

이름: 김 민 성

최근, 이미지 수집, 이미지 데이터 처리가 사용되는 휴대용 전자기기, 머신 비전 분야에서 광시야각, 적은 수차, 높은 신호 대 잡음비 등을 가지는 효율적이고 고품질의 물체감지 시스템을 개발하기 위한 이미지 센서 기술이 크게 관심을 받고있다. 하지만, 기존의 카메라는 평면형 이미지 센서를 사용하기 때문에, 넓은 시야각에서 들어오는 이미지를 수차 없이 수집하기 위해서는 다중 렌즈 구조가 필수적이다. 이러한 다중 렌즈 구조는 제작하는 비용이 비싸며, 사용되는 전자기기의 소형화를 어렵게 한다. 이러한 맥락에서, 서식 환경에 최적화되도록 진화했으며, 단일 수정체와 굴곡진 망막으로 이루어진 동물들의 눈을 모방하면 소형화가 어렵다는 기술적인 한계를 효율적으로 해결할 수 있다. 또한 고품질의 시각 정보를 얻기 위한 그들만의 이미지 수집 전략을 모방하여, 높은 물체 감지율과 높은 신호 대 잡음비를 가지는 특수한 카메라를 개발 할 수 있다. 이 논문에서는, 우리가 개발한 세 가지 종류의 차세대 생체 모방 카메라를 설명하려고 한다.

먼저, 수중생물의 눈에서 영감을 얻어, 모노센트릭렌즈와 반구형 실리콘 나노로드 포토다이오드 어레이를 결합하여 초소형, 광시야각, 깊은심도, 손쉬운 초점조정 그리고 향상된 빛 감도를 가지는 카메라를 개발하였다.

이론적인 분석과 실험적인 검증을 통하여 개발된 생체모방 카메라를 이용하여 고품질의 광시야각 이미지를 성공적으로 얻을 수 있었다.

다음으로, 얕은 물에 서식하는 갑오징어의 눈에서 영감을 받아, 저대비 환경에 특화된 고대비 고해상도 편광 카메라를 개발하였다. W 모양의 동공을 모방하여, 수직방향으로 불균일한 입사광선을 균일하게 분포되도록 조절했고, 고밀도의 슬릿 형태의 픽셀을 포함하는 원통형 실리콘 포토다이오드 어레이를 사용하여, 넓은 수평방향의 시야각을 가지도록 했다. 또 유연한 편광 필름을 원통형 실리콘 포토다이오드 어레이 위에 부착하여, 고대비 편광 이미징이 가능하도록 하였다.

마지막으로, 사람의 시각 인식 시스템의 구조적 및 기능적 특징에서 영감을 받아, MoS_2 와 poly(1,3,5-trimethyl-1,3,5-trivinyl cyclotrisiloxane) 의 이종 구조를 사용한 노이즈가 감소된 곡면형 뉴로모픽 이미지 센서 어레이를 개발하였다. 실험적 및 이론적으로 분석한 MoS2-pV3D3 광트랜지스터의 광자 유발 시냅스 가소성을 활용하여, 노이즈가 많은 입사 이미지들을 받아, 노이즈가 감소된 이미지를 출력하여 고유 이미지를 효율적으로 인식 할 수 있는 시스템을 개발하였다.

주요어: 생체 모방 인공 시각, 인공 시냅스, 특화 카메라, 곡면형 이미지센서, 뉴로몰픽 시각 센서, 유연 전자 소자